Magneto-Structural Transition and Refrigeration Property in All-D-Metal Heusler Alloys: A Critical Review

Qinyu Zhang, Mingfang Qian* and Xuexi Zhang*

School of Materials Science and Engineering, Harbin Institute of Technology, Harbin 150001, China

Abstract: All-d-metal Heusler alloys has attracted much attention due to its unique magnetic properties, martensite transformation behavior and related solid-state refrigeration performance. These unique type alloys are recently discovered in 2015 and have been widely studied; however, systematic reviews on their magneto-structural transition and refrigeration property are rare. In this review, we first summarize the preparation techniques and microstructure of the bulk alloys and ribbons. Then the magnetic transition and martensite transformation behavior are reviewed, focusing on the correlation between magneto-structural transition and refrigeration properties. The effects of element doping, external magnetic and mechanical fields on the martensite transformation and corresponding magnetic entropy change are summarized. We end this review by proposing the further development prospective in the field of all-d-metal Heusler alloys.

Keywords: All-d-metal Heusler alloys, Microstructure, Magneto-structural transition, Magnetic properties, Magnetic refrigeration.

1. INTRODUCTION

Heusler alloys, first discovered by Fritz Heusler in 1903, have attracted much attention due to their unique physical and chemical properties. Currently, Heusler-type alloys are promising candidate materials for various fields, such as actuation [1], energy conversion [2-4], refrigeration [5-12], catalysis [13, 14] and so on [15-20].

The element constituents and crystal structure of traditional Heusler alloys with X_2YZ formula are shown in Figure **1**. In generally, X and Y are d-group transition metal elements, while Z is p-group main elements [21-23]. Heusler alloys usually exhibit two different crystal structures: Cu_2MnAl-type (No. 225) and Hg_2CuTi-type (No. 216). The covalent bond formed via p-d orbital hybridization between p- and d-group atoms may stabilize the parent phase [24]. On the other hand, such covalent bond is prone to induce the poor mechanical properties (especially the low ductility), which greatly limited their practical applications [7, 11, 25].

A variety of approaches have been employed to improve the mechanical properties of Heusler alloys [7, 8, 26-40]. In 2015, Wei *et al.* [41] prepared a kind of novel Heusler alloys by replacing p-group atoms with third transition metal atoms. The created alloys only contain d-group elements and thus are named all-d-metal alloys, which show enhanced mechanical properties and thus attracted much attention in recent years.

Up to now, great progress has been made in the field of all-d-metal Heusler alloy. However, critical review on this field is still lack. In this brief review, we first summarized the preparation methods and microstructure of all-d-metal Heusler alloys. Then the factors affecting the martensite/magnetic transitions and mechanical/magnetic/magnetocaloric properties were reviewed. Finally, the development prospective of all-d-metal Heusler alloys was provided.

2. PREPARATION AND MICROSTRUCTURE OF ALL-D-METAL ALLOYS

Different methods have been employed to prepare different all-d-metal alloys [12, 41-55]. Meanwhile, their microstructures were characterized by a lot of technique, including optical microscopy (OM), scanning electron microscopy (SEM), electron backscattered diffraction (EBSD) and transmission electron microscopy (TEM).

All-d-metal bulk alloy ingots are usually prepared by arc-melting under inert gas atmosphere. The microstructure of $Ni_{40}Cu_{10}Mn_{35}Ti_{15}$ and $Ni_{37}Co_{13}Mn_{34.5}Ti_{15.5}$ alloy ingots is displayed in Figure **2** [42, 56]. The as-cast $Ni_{40}Cu_{10}Mn_{35}Ti_{15}$ alloy exhibited typical cellular structure (Figure **2a**), different with the globular microstructure of the cast $Ni_{37}Co_{13}Mn_{34.5}Ti_{15.5}$ alloy (Figure **2c**). The different microstructure was

*Address correspondence to this author at the School of Materials Science and Engineering, Harbin Institute of Technology, Harbin 150001, China;
E-mail: mingfang.qian@hit.edu.cn, xxzhang@hit.edu.cn

E-ISSN: 2410-2199/22

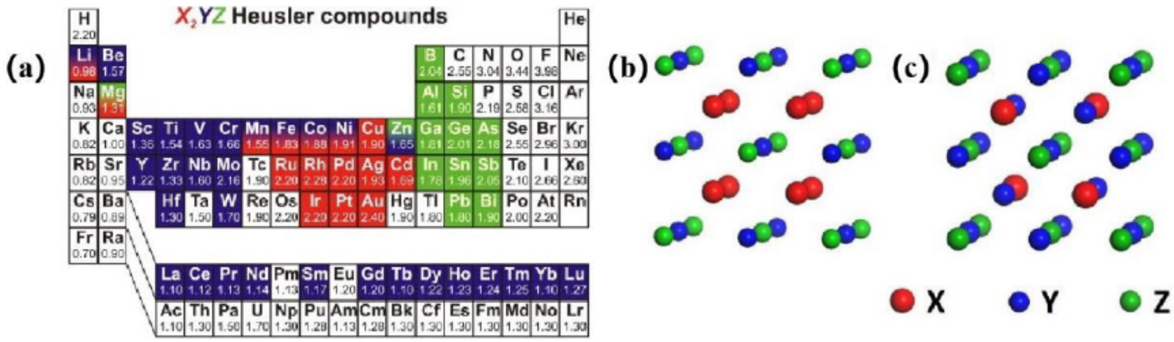

Figure 1: Constituents and structure of Heusler alloys [21]. (**a**) Element constituents; (**b**) Cu_2MnAl-type structure; (**c**) Hg_2CuTi-type structure.

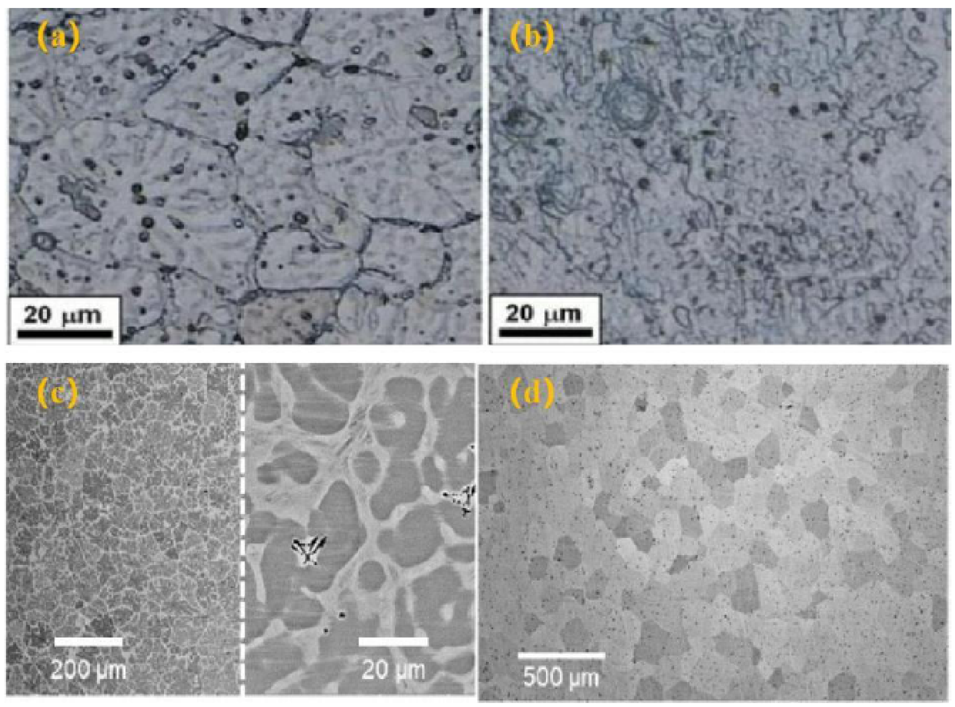

Figure 2: Microstructure of all-d-metal bulk alloys [42, 56]. (**a**) As-cast and (**b**) annealed $Ni_{40}Cu_{10}Mn_{35}Ti_{15}$, (**c**) As-cast and (**d**) annealed $Ni_{37}Co_{13}Mn_{34.5}Ti_{15.5}$.

related to the different solidification rates. Compared with the as-cast state, the annealed alloys (Figure **2b** and d) show better chemical homogeniety on the microscopic scale, which is beneficial for the functional properties of materials [41].

All-d-metal alloy ribbons can be prepared by melt-spinning technique [47-53]. The typical microstructure of $Ni_{36.0}Co_{14.0}Mn_{35.7}Ti_{14.3}$ ribbons is shown in Figure **3** [49]. The martensite and equiaxed-grain-like austenite can be observed on the free surface of the ribbon (Figure **3a**), indicating that the martensite transformation (MT) of the ribbon takes place at ambient temperature. Comparison of the melt-spun and annealed ribbons in Figure **3a** and **b** shows that the average grain size slightly increased after annealing, as illustrated in Figure **3c** and **d**. Depicted in Figure **3e** and **f** is the corresponding fracturing cross-section images of melt-spun and annealed ribbons, revealing that columnar grains perpendicular to the free surface are created.

On the other hand, all-d-metal Heusler alloys film can be well prepared by direct-current (DC) double targets magnetron co-sputtering method [54, 55]. In this technique, the MgO (100) substrate was often used. Figure **4** demonstrates the typical microstructures of Ni-Co-Mn-Ti all-d-metal Heusler

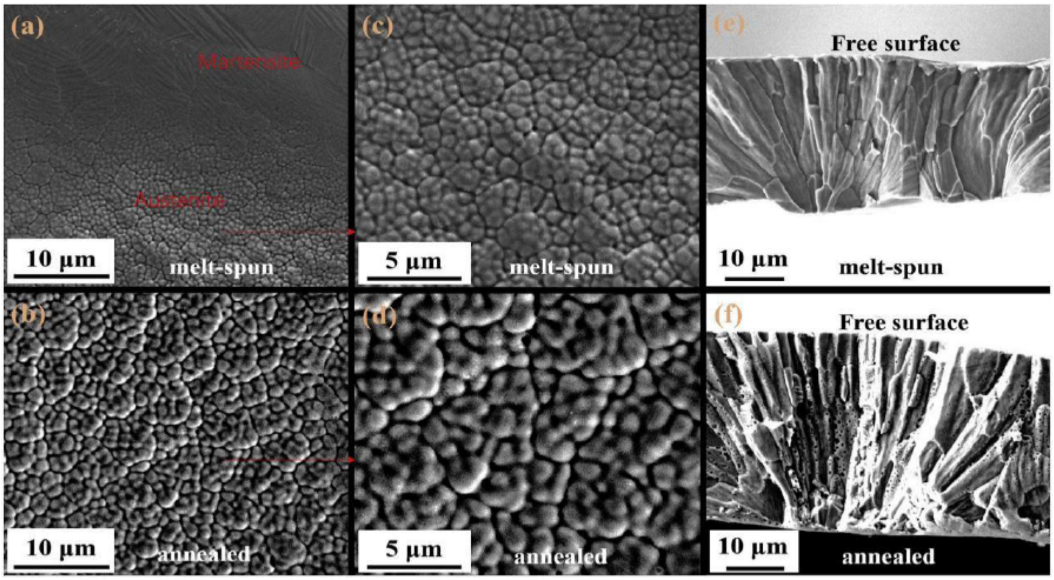

Figure 3: Microstructures of all-d-metal $Ni_{36.0}Co_{14.0}Mn_{35.7}Ti_{14.3}$ alloy ribbons. (**a,c**) Free surfaces of melt-spun ribbons; (**b,d**) Free surfaces of annealed ribbons; (**e**) Cross sections of melt-spun ribbons; (**f**) Cross sections of annealed ribbons. Free surface: free solidification side surface far away from copper roller [49].

alloys film [55]. From the surface images, the agglomeration and contrast among particles indicate that the films grow in island mode (Volmer-Weber mode), in which the grains produce different heights. It is obvious that the average grain size increases with increasing deposition temperature (DT). The average grain size for $Ni_{40.5}Co_{14.1}Mn_{31.6}Ti_{13.8}$ (sample A), $Ni_{40.6}Co_{14.1}Mn_{31.5}Ti_{13.8}$ (sample C), and $Ni_{39.3}Co_{15.3}Mn_{31.8}Ti_{13.6}$ (sample D) are about 21.5(6) nm, 36.5(1) nm and 85.5(0) nm, respectively. In addition, a lot of small grains are also observed in Figure **4c** and **e**. These small grains may be formed by pure Ni, Co, Mn or Ti elements, implying that the Ar ions on the surface may possibly hinder the diffusion of sputtered atoms on the surface. From the fracture cross-section of films (Figure **4b**, **d** and **f**), sample A, C and D have a thickness of ~620, ~670 and ~700 nm, respectively. This shows that the film thickness slightly increase with the increasing DT.

3. MAGNETO-STRUCTURAL TRANSITION AND PROPERTIES OF ALL-D-METAL ALLOYS

All-d-metal Heusler alloys have many fascinating multifunctional properties, which are related to the MT from high-temperature austenite to low-temperature martensite phases [48-51, 53-55, 57, 58]. Therefore, the factors affecting the MT play an important role in the properties and applications of all-d-metal Heusler alloys.

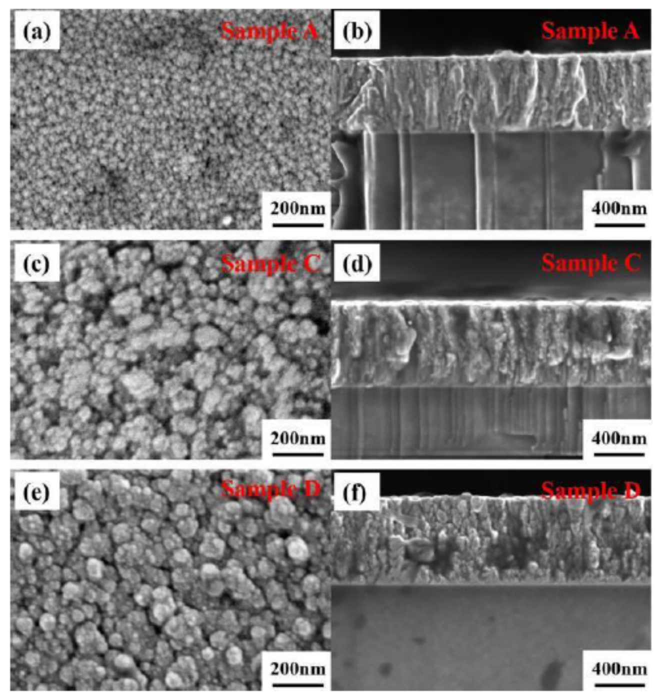

Figure 4: SEM images showing the surfaces and cross sections for (**a**, **b**) $Ni_{40.5}Co_{14.1}Mn_{31.6}Ti_{13.8}$ (sample A), (**c**, **d**) $Ni_{40.6}Co_{14.1}Mn_{31.5}Ti_{13.8}$ (sample C) and (**e**, **f**) $Ni_{39.3}Co_{15.3}Mn_{31.8}Ti_{13.6}$ (sample D). The grain size increases with increasing DT. The cross-section images show the thickness is almost the same for all samples, indicating that DT has little effect on the thickness of the films [55].

Wei *et al*. [41] prepared the $Ni_{50}Mn_{50-y}Ti_y$ (y = 0, 6, 9, 12, 15, 20, 25, 30, denoted as Ti_y) and $Mn_{50}Ni_{50-y}Ti_y$ (y = 0, 6, 9, 10, 11, 12, 15) alloys by arc-melting high purity metals in argon atmosphere. In Figure **5a**, the

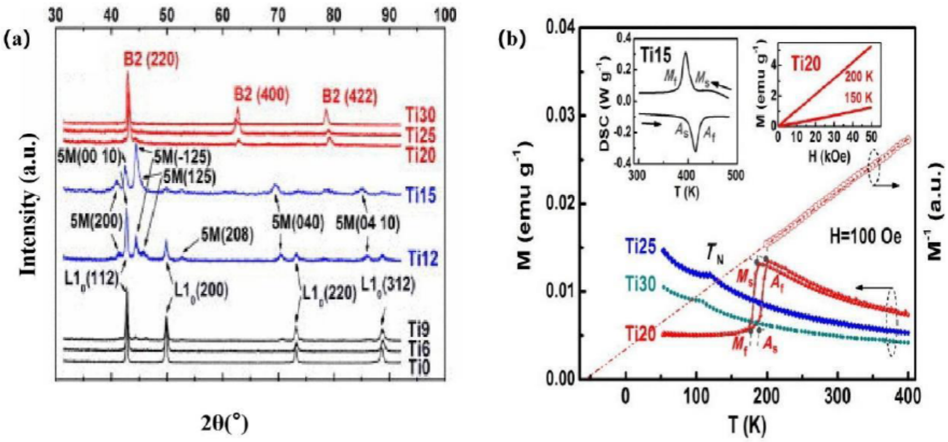

Figure 5: Phase and magnetic properties of $Ni_{50}Mn_{50-y}Ti_y$ (y = 0, 6, 9, 12, 15, 20, 25, 30) alloys. (**a**) Room-temperature X-ray diffraction (XRD) patterns at ambient temperature; (**b**) Temperature dependent magnetization (M-T) curves for $Ni_{50}Mn_{50-y}Ti_y$ (y = 20, 25, 30) alloys and M^{-1}-T plot for Ti20. The left inset in (**b**) shows the differential scanning calorimetry (DSC) result for $Ni_{50}Mn_{35}Ti_{15}$ alloy, and the right inset in (**b**) is the magnetic isotherms of Ti20 at temperatures well above and below T_M. M_s and M_f refer to the starting and finishing temperatures of forward MT, respectively. A_s and A_f are the starting and finishing temperatures of inverse MT, respectively [41].

$L1_0$ martensite phase exists in the low-Ti-content alloys (Ti0, Ti6 and Ti9) at room temperature (RT), only austenite phase is observed for high-Ti-content alloys (Ti20, Ti25 and Ti30). Coexistence of different martensite phases ($L1_0$ and 5M) exists in medium-Ti-content alloys (Ti12 and Ti15). The MT temperature of $Ni_{50}Mn_{50-y}Ti_y$ alloys decreases with increasing Ti content. For Ti20 (Figure **5b**), the thermal hysteresis of 181-194 K is observed. Meanwhile, the fact that a linear fit of M^{-1}-T above the MT with a negative extrapolated temperature confirms the antiferromagnetic (AFM) character of the austenite. The linear magnetic isotherms at temperature of 200 K (austenite) and 150 K (martensite) (right inset of Figure **5b**) indicate paramagnetic (PM) behavior of the austenite and FM behavior of the martensite, respectively This type of magneto-structural MT between high- and low-temperature PM phases differs significantly from the first-order magnetic transition (FOMT) in some other materials, such as Gd-Si-Ge [55].

Currently, the main factors affecting the actual applications of all-d-metal alloys are low mechanical toughness and limited functional properties, partially related to defects during fabrication [41, 43]. Some strategies have been proposed to overcome these problems, including (a) element doping, (b) microstructure adjustment (texture and reducing sample size) and (c) multi-field cooperation. Of course, researches could apply these strategies based on actual demands.

3.1. Element Doping

(1) Magnetic element doping. The strong ferromagnetism was not established by introducing Ti in the Ni-Mn-Ti and Mn-Ni-Ti all-d-metal Heusler alloys. Wei *et al*. [41, 43] applied the "ferromagnetic (FM) activation effect" of the Co atom to induce the ferromagnetic transition in Ni-Mn-Ti and Mn-Ni-Ti alloys. The abrupt magnetic transitions corresponding to MT from strong FM austenite to weak-magnetic (PM or AFM) martensite can be seen in Figure **6**. It shows that metamagnetic martensite transformation exists in Co-doped Ni-Mn-Ti and Mn-Ni-Ti alloys.

Figure **7** demonstrates the magnetic and magneto-responsive properties across the MT of a $Ni_{35}Co_{15}Mn_{35}Ti_{15}$ alloy [41]. A large magnetization difference (ΔM) about 90 emu g^{-1} is associated with MT transformation (Figure **7a**), which facilitates transformation-related magneto-responsive effects. Magnetic isotherms across the MT are shown in Figure **7b**. At 290 K, the austenite reveals typical FM behavior. The isotherms at lower temperatures of 235, 253 and 270 K exhibit a clear metamagnetic behavior (*i.e*. magnetic-field induced reverse MT from weak-magnetic martensite to strong-ferromagnetic austenite) with pronounced magnetic hysteresis. Especially, at 253 K a two-way reversible MT is observed. Figure **7c** shows the field dependence of the strain. At 253 K, the strain saturates with a maximum value of 2400 ppm in a magnetic field of 120 kOe. This large magneto-strain originates from cell volume expansion due to the field-induced reverse MT. The strain recovery during decrease of the field indicates magnetic superelasticity

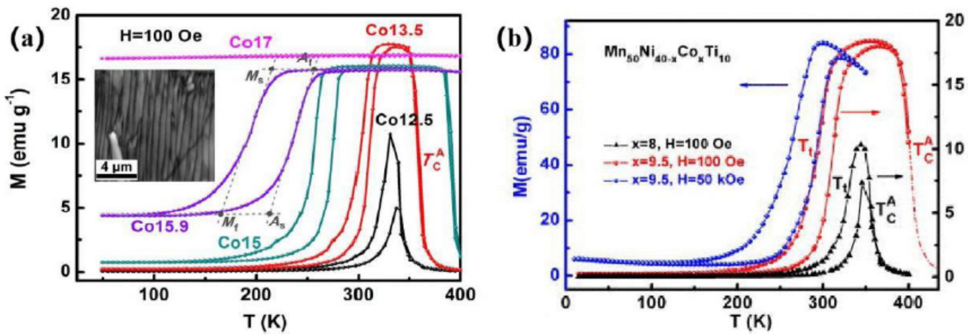

Figure 6: M-T curves of (**a**) $Ni_{50-x}Co_xMn_{35}Ti_{15}$, (**b**) $Mn_{50}Ni_{40-x}Co_xTi_{10}$ alloys [41, 43].

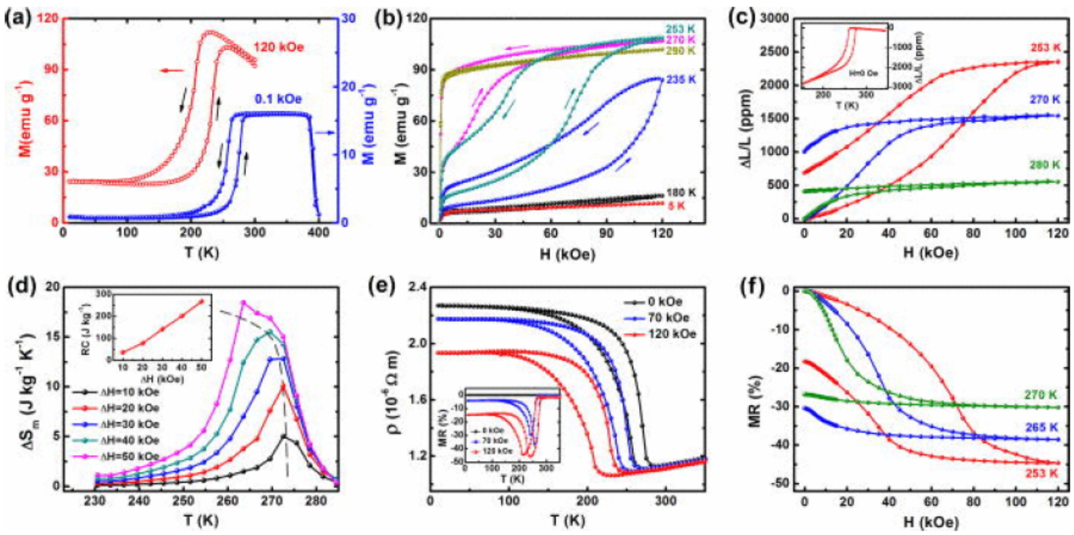

Figure 7: Magnetic and magneto-responsive properties across the MT of the $Ni_{35}Co_{15}Mn_{35}Ti_{15}$ alloy. (**a**) Temperature dependence of the magnetization in magnetic fields of 0.1 and 120 kOe; (**b**) Magnetic isotherms at several temperatures; (**c**) Field-induced strain at several temperatures. The inset shows the temperature dependence of the strain; (**d**) Magnetic-entropy change (ΔS_m) at various field changes. The inset shows the refrigerating capacity (RC); (**e**) Temperature dependence of the electrical resistivity in magnetic fields of 0, 70, and 120 kOe. The inset shows the temperature dependence of the magnetoresistance (MR); (**f**) Field dependence of the MR at various temperatures [41].

of the alloy. The magnetic entropy changes (ΔS_m) were calculated using Maxwell relation, as shown in Figure **7d**. A maximum ΔS_m value around 18 J kg^{-1} K^{-1} is obtained at about 263 K under a field change of 50 kOe. The obtained ΔS_m is comparable to that of many other Heusler alloys. The inset of Figure **7d** shows the refrigeration capacity (RC), which has a relatively high value of 267 J kg^{-1} under 50 kOe. This shows that the Co-doped all-d-metal Heusler FSMAs may have a potential as magnetocaloric materials.

The MT is accompanied by an electrical resistance change. To investigate this effect, the temperature dependence of the electrical resistance was measured in various magnetic fields, as shown in Figure **7e**. The electrical resistance exhibits abrupt jump across the FMMT due to intrinsic changes of both the anisotropy and the area of the Fermi surface caused by the lattice distortion. A remarkable shift of the jump onset with increasing field towards lower temperatures is related to the field-induced FMMT. As illustrated in the inset of Figure **7e**, large magnetoresistance (MR) values of 37% at 70 kOe and 46% at 120 kOe are found across MT. The field dependent MR at different temperatures is shown in Figure **7f**, which is consistent with the field dependence of the strain.

(2) Cu doping. De Paula *et al*. [56] prepared the $Ni_{40}Cu_{10}Mn_{35}Ti_{15}$ alloy and investigated its magnetic, electronic, and mechanical properties after thermal annealing. Compared with $Ni_{50}Mn_{35}Ti_{15}$ in the inset of Figure **5b**, it was observed that the MT temperature of $Ni_{40}Cu_{10}Mn_{35}Ti_{15}$ decreased due to the doping of Cu (inset of Figure **8a**). In Figure **8a**, an antiferromagnetic ordering transition with large thermal hysteresis takes place for both the annealed and as-cast samples, suggesting the presence of MT in this alloy. The

magnetic phase transition from the paramagnetic to the antiferromagnetic state is also strongly correlated with the electric resistivity. Figure **8b** shows abrupt increase in resistivity values in both samples as temperature decreases below 154 K. In fact, the sharp increase in electrical resistivity across the MT is a common feature in conventional Ni-Mn-based Heusler alloys. This feature is attributed to the changes in the atomic bond length of Ni and Mn atoms due to symmetry reduction across MT, which alters the density of states near the Fermi level. In addition, no cracks appear at the indentation corners of the annealed $Ni_{40}Co_{10}Mn_{35}Ti_{15}$ samples after Vickers micro-hardness indentation (Figure **8b**), revealing that the sample may possibly has good toughness.

(3) B doping. Boron element was usually used to enhance the grain boundary strength and thus improve the mechanical properties [12, 46]. Cong *et al*. [46] synthesized $(Ni_{50}Mn_{31.5}Ti_{18.5})_{99.8}B_{0.2}$ alloys and investigated its elastocaloric effect (eCE) and crystal structure. Micro-alloying with B leads to decreasing transformation temperature in Figure **9a**. Figure **9b** shows that the MT of $(Ni_{50}Mn_{31.5}Ti_{18.5})_{99.8}B_{0.2}$ alloy occurs between paramagnetic austenite and paramagnetic martensite. The adiabatic temperature change (ΔT_{ad}) and isothermal entropy change (ΔS_{iso}) are two important parameters for eCE. The ΔT_{ad} (Figure **9c**) and ΔS_{iso} (Figure **9d**) are 31.5 K and 45 J kg^{-1} K^{-1}, respectively. To better understand the colossal

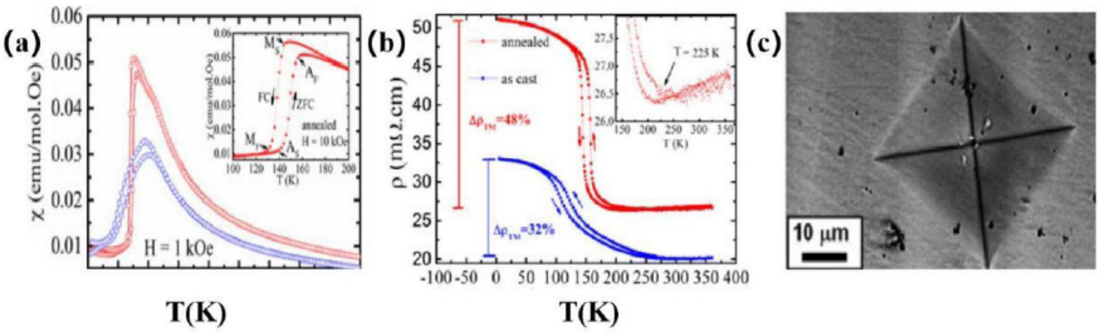

Figure 8: Magnetization properties and indentation of $Ni_{40}Cu_{10}Mn_{35}Ti_{15}$ alloys [56]. (**a**) DC magnetic susceptibility of as-cast and annealed alloys, following ZFC/FC protocols under the applied magnetic field of 1 kOe. The inset is the MT temperatures at 10 kOe for the annealed alloy; (**b**) Temperature dependence of DC electrical resistivity of the As-cast and annealed alloys; (**c**) SEM-BSE images showing the micro-hardness indentation.

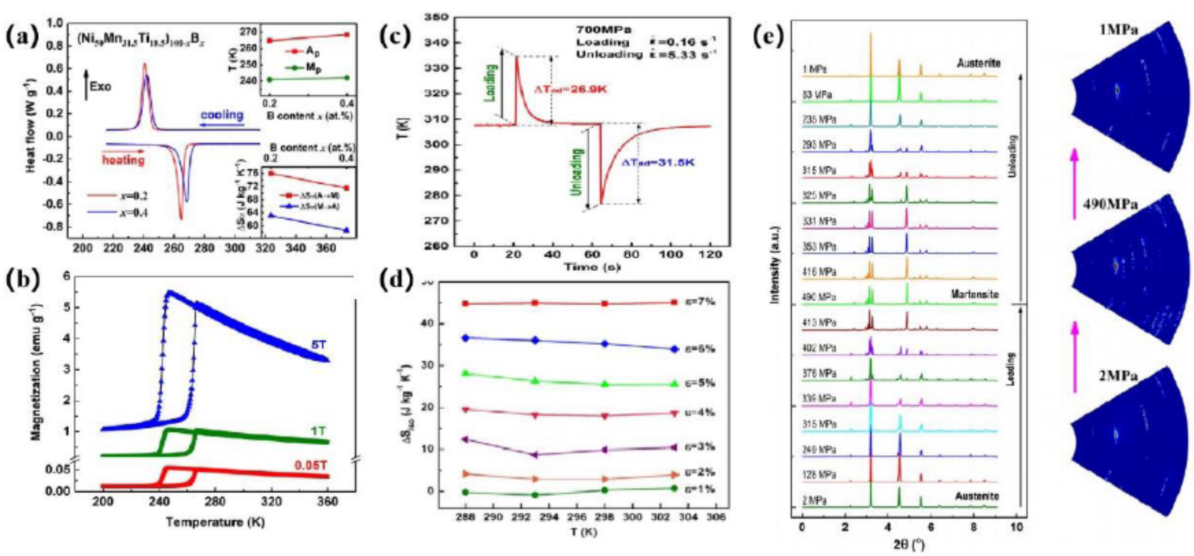

Figure 9: Phase transitions of boron-microalloyed $(Ni_{50}Mn_{31.5}Ti_{18.5})_{100-x}B_x$ alloys [46]. (a) DSC curves of $(Ni_{50}Mn_{31.5}Ti_{18.5})_{100-x}B_x$ alloys; (b) M-T curves of $(Ni_{50}Mn_{31.5}Ti_{18.5})_{99.8}B_{0.2}$ alloy under constant magnetic fields of 0.05, 1 and 5 T; (c) Colossal adiabatic temperature change in $(Ni_{50}Mn_{31.5}Ti_{18.5})_{99.8}B_{0.2}$ alloy; (d) Isothermal entropy change as a function of temperature at different strain levels; (e) Crystal structure evolution during stress-induced transformation in $(Ni_{50}Mn_{31.5}Ti_{18.5})_{99.8}B_{0.2}$. (Left) 1D HEXRD patterns at different stress levels during loading and unloading at 295 K. (Right) Representative zone of the 2D HEXRD patterns collected before loading (2 MPa), at the maximum stress (490 MPa), and after unloading (1 MPa) at 295 K.

eCE and its underlying mechanism, an in-situ synchrotron HEXRD experiment was performed to trace the structural evolution during loading and unloading processes. As displayed in Figure **9e**, the sample exhibits austenite structure (No. 225) before loading. Upon applying an external stress, it transforms into an orthorhombic (No. 51) martensite. Notably, the stress-induced MT is fully accomplished when the stress reaches 413 MPa. During unloading, the stress-induced martensite fully transforms back to austenite. 2D HEXRD patterns (right of Figure **9e**) collected before and after loading are almost identical, indicating that the stress-induced transformation is fully reversible. The good reversibility of the stress-induced transformation is important for colossal reversible eCE. Aznar *et al*. [12] also prepared $(Ni_{50}Mn_{31.5}Ti_{18.5})_{99.8}B_{0.2}$ alloys with giant barocaloric effect (BCE), which shows ΔT_{ad} and ΔS_{iso} of 12 K and 74 J kg^{-1} K^{-1}, respectively.

3.2. Introduction of Texture During Fabrication

Texture structure was usually used to improve the mechanical properties [36]. Yan *et al*. [44] fabricated <100>-textured $Ni_{50}Mn_{31.75}Ti_{18.25}$ bulk alloy by arc-melting and directionally solidification technique. The critical temperatures of MT (Figure **10a**), *i.e*., M_s, M_f, A_s and A_f, were determined by tangent method to be 254.8, 225.7, 240.1 and 272.2 K, respectively. The thermal hysteresis ΔT_{Hys} (*i.e*. $[(A_s + A_f) - (M_s + M_f)] / 2$) and phase transition interval ΔT_{Int} (*i.e*. $[(M_s - M_f) + (A_f - A_s)] / 2$) that describe the reversibility of structural transition, are 15.9 and 30.6 K, respectively. Figure **10b** shows similar results in $Ni_{50}Mn_{50-y}Ti_y$ and $Mn_{50}Ni_{50-y}Ti_y$ alloys, which exhibit MT between paramagnetic austenite and paramagnetic martensite. Figure **10c** shows the time dependence of ΔT_{ad} with an applied strain of 10%. A giant ΔT_{ad} of −20.4 K is detected during reverse MT. In Figure **10d**, the ultimate compressive strain and stress of the <100>-textured $Ni_{50}Mn_{31.75}Ti_{18.25}$ alloy are determined to be ~13% and ~1.1 GPa, respectively. As a result of the existence of texture structure, the alloy shows largely enhanced fracture resistance in comparison with that of conventional Ni-Mn-based alloys [30, 59-62].

3.3. Combination of Doping and Reducing Material Size

Liu *et al*. [48] prepared the all-d-metal $Ni_{50-x}Co_xMn_{35}Ti_{15}$ (x = 13,13.5) ferromagnetic alloy ribbons

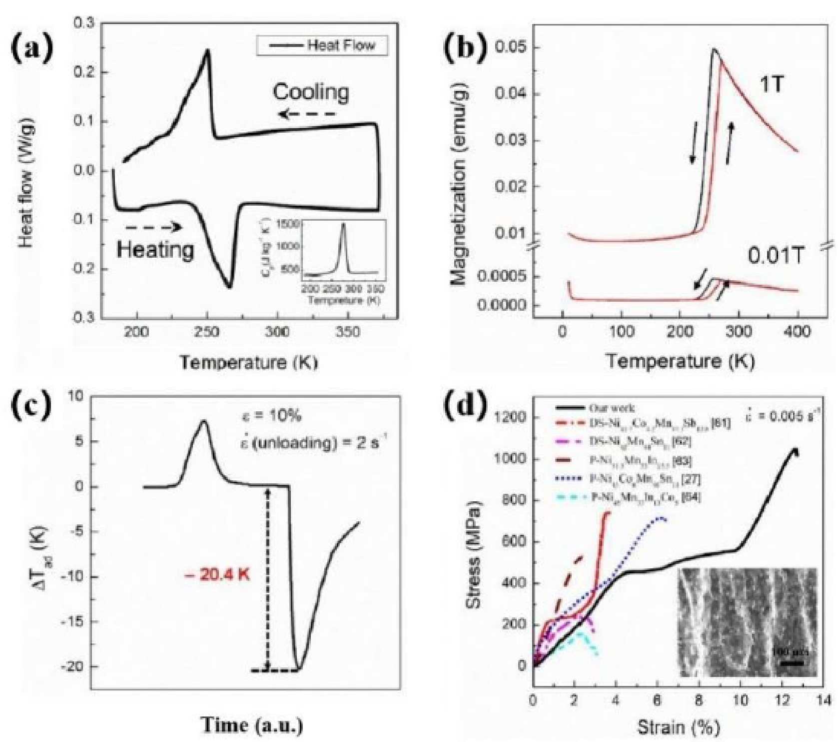

Figure 10: Martensite transformation, magnetic and mechanical properties of $Ni_{50}Mn_{31.75}Ti_{18.25}$ alloy. (**a**) DSC curve of directionally solidified alloy with <100>-texture; (**b**) M-T curves of under magnetic fields of 0.01 and 1 T; (**c**) Time dependence of ΔT_{ad} in the sample with an applied strain of 10%; (**d**) Comparison of the fracture curves of the <100>-textured $Ni_{50}Mn_{31.75}Ti_{18.25}$ alloy with that of the conventional Ni-Mn-based alloys. “DS” and “P” represent the directionally solidified and the casted polycrystalline samples, respectively. The inset is the fracture surface of the studied alloy [44].

via arc-melting and subsequent melt-spinning techniques under Ar atmosphere. The phase transition and correlative properties of ribbon samples were investigated. Compared to the structure (only B2-type) of melt-spun ribbon at RT, Figure **11a** shows the coexistence of three different phases ($L1_0$, 5M, B2) in the annealed $Ni_{36.5}Co_{13.5}Mn_{35}Ti_{15}$ ribbons, implying that the intermartensite transformation (IMT) exists and MT shifts markedly to higher temperatures after annealing at 850 °C. The critical temperatures of MT in annealed $Ni_{36.5}Co_{13.5}Mn_{35}Ti_{15}$ alloy ribbon (Figure **11b**), *i.e.*, M_s, M_f, as and A_f, are determined to be 306.5, 284, 8, 311.6 and 327.2 K, respectively. The thermal hysteresis ΔT_{Hys} and phase transition interval ΔT_{Int} are 23.8 and 32.6 K, respectively. Figure **11c** shows M-T curves of annealed ribbon under applied fields $\mu_0 H$ of 0.1 and 5 T. With further decreasing temperature, an abrupt drop of magnetization indicates the occurrence of MT from FM parent phase to weak-magnetic martensite. Meanwhile, the increase in applied filed from $\mu_0 H$ = 0.1-5 T leads to the shifts of MT to lower temperatures. Under the applied fields $\mu_0 H$ of 5 T during reverse MT, the ΔM (Figure **11c**), ΔS_m (Figure **11d**) and RC (inset of Figure **11d**) are 86.9 $Am^2\ kg^{-1}$, 24.9 $J\ kg^{-1}\ K^{-1}$ and 239.7 $J\ kg^{-1}$, respectively. As illustrated in Figure **11e**, quite large MR value of 34.9% at 5T is found across the transformation. Figure **11f** manifests the excellent mechanical properties of the annealed ribbon in contrast to some steel materials [63-65].

Neves Bez *et al*. [50] found that the peak value of ΔS_m decreases with increasing Co content in the $Ni_{50-x}Co_xMn_{35}Ti_{15}$ (12.5<x <15) alloy ribbon (Figure **12a**). More interestingly, the ΔS_m of the $Ni_{37.5}Co_{12.5}Mn_{35}Ti_{15}$ ribbon is 400% higher than that of the bulk alloy (Figure **12b**). The enhanced ΔS_m may be attributed to the presence of high degree of chemical homogeneity in the ribbon. Zeng *et al*. [53] fabricated the $Ni_{50-x}Fe_xMn_{35}Ti_{15}$ alloy ribbons by introducing Fe element in Ni-Mn-Ti alloy and discussed the effect of Fe element on MT. The XRD (Figure **13a**) and DSC (Figure **13b**) indicate that Fe substitution efficiently decreases the transformation temperature by stabilizing the B2 parent phase. For $Ni_{32}Fe_{18}Mn_{35}Ti_{15}$ alloy ribbon, the transformation temperatures of the forward and reverse MT are determined to be 192 and 208 K, respectively. Figure **13c** shows that FMMT has been realized in $Ni_{32}Fe_{18}Mn_{35}Ti_{15}$ alloy ribbon. The role of Fe element is similar to that of Co element. Under an applied field $\mu_0 H$ of 5 T during reverse MT, the ΔM (Figure **13c**) and ΔS_m (Figure **13d**) of $Ni_{32}Fe_{18}Mn_{35}Ti_{15}$ alloy ribbon are 35 $Am^2\ kg^{-1}$ and 12.5 $J\ kg^{-1}\ K^{-1}$, respectively. The MR (Figure **13e**) and anomalous Hall effect (Figure **13f**) are observed across the transformation. Li *et al*. [51]

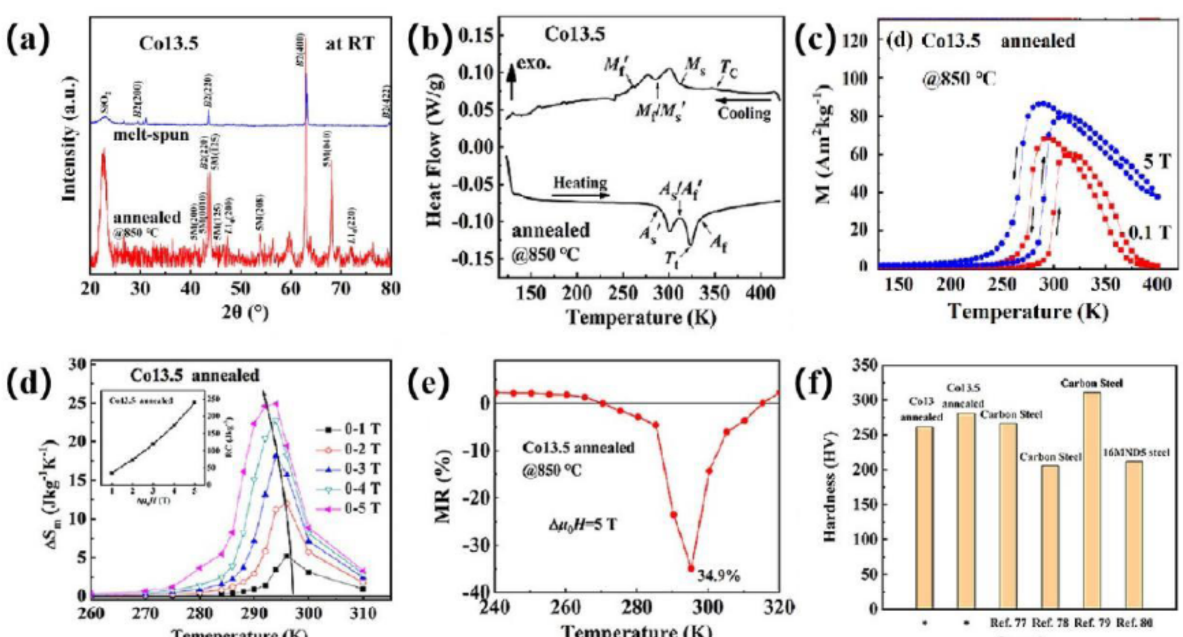

Figure 11: Phase transition, magnetic property and properties of $Ni_{36.5}Co_{13.5}Mn_{35}Ti_{15}$ alloy ribbons [48]. (**a**) Room-temperature XRD patterns for melt-spun and annealed (at 850 ℃) ribbons; (**b**) DSC curves for annealed ribbon; (**c**) M-T curves of annealed ribbon under applied fields $\mu_0 H$ of 0.1 and 5 T; (**d**) ΔS_m(T) curves of annealed ribbon under different field changes $\Delta\mu_0 H$ of 0-1, 2, 3, 4, 5 T. The corresponding insets show the magnetic field change dependence of RC; (**e**) Magnetoresistance of annealed ribbon under magnetic field change $\Delta\mu_0 H$ 0-5 T; (**f**) Vickers hardness of annealed ribbon and some other well-studied steels.

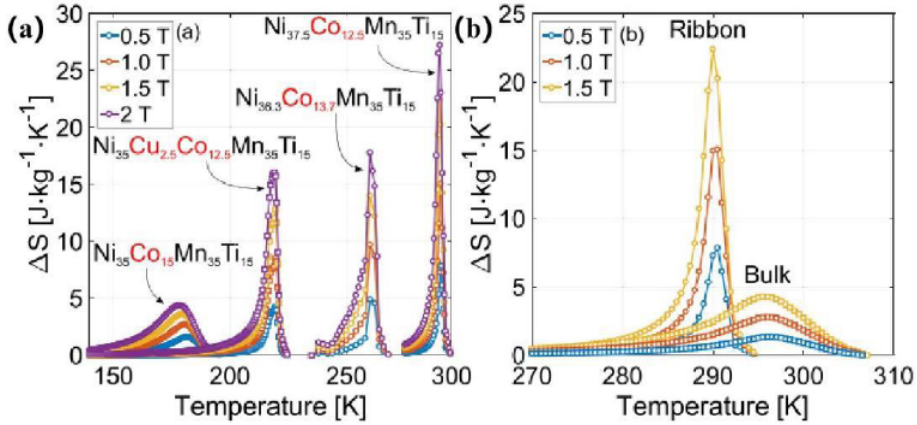

Figure 12: Magnetic entropy change of $Ni_{37.5}Co_{12.5}Mn_{35}Ti_{15}$ ribbons [50]. (**a**) Temperature dependence of ΔS_m; (**b**) ΔS_m of $Ni_{37.5}Co_{12.5}Mn_{35}Ti_{15}$ ribbons and bulk alloys under various magnetic field changes.

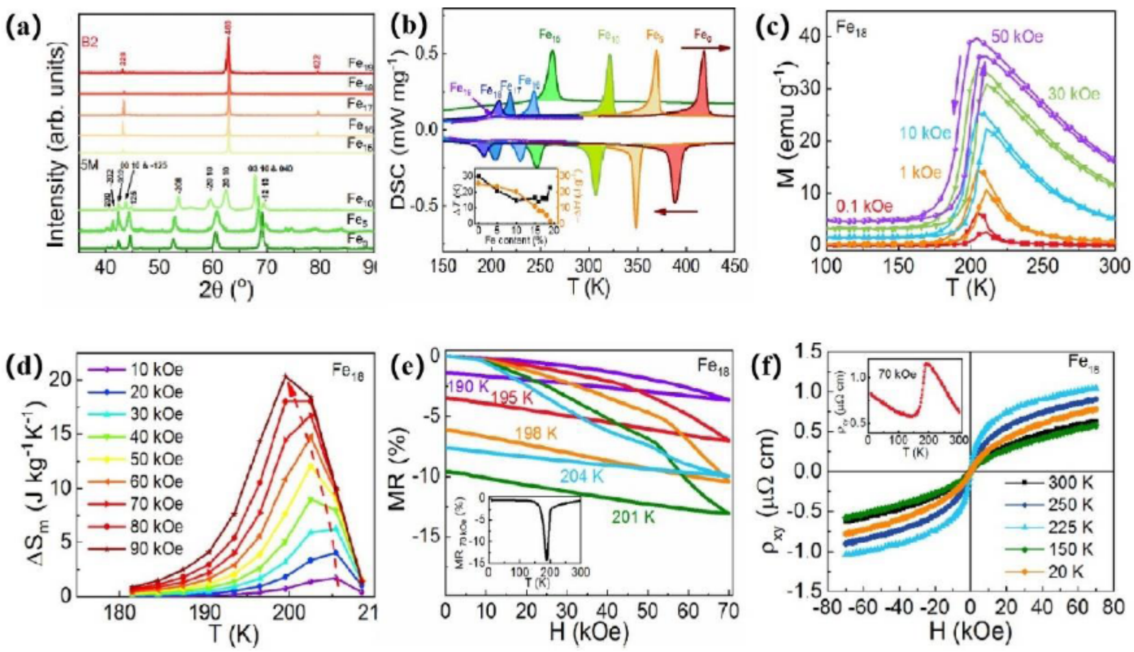

Figure 13: Microstructure and properties of $Ni_{50-x}Fe_xMn_{35}Ti_{15}$ (denoted as Fe_x) ribbons [53]. (**a**) Room temperature XRD patterns; (**b**) DSC measurements for the MT. The insert shows hysteresis (ΔT) dependence on Fe content and latent heat (ΔH) obtained from DSC; (**c**) M-T curves of Fe_{18} sample under different magnetic fields; (**d**) Temperature dependence of the magnetic entropy changes (ΔS_m) with magnetic fields 10-90 kOe; (**e**) Magnetic field dependence of MR at various temperatures of Fe_{18}. The insert is the temperature dependence MR under a magnetic field of 70 kOe; (f) Magnetic field dependence of Hall resistivity ρ_{xy} at various temperatures of Fe_{18}. The insert is the temperature dependence of ρ_{xy} in 70 kOe.

investigated the influence of different Co/Fe ratio on the crystal structure, FMMT and magnetocaloric effect (MCE) of $Ni_{35}Co_{15-x}Fe_xMn_{35}Ti_{15}$ (x = 2, 4, 6, 8) alloy ribbons.

All the $Ni_{35}Co_{15-x}Fe_xMn_{35}Ti_{15}$ alloys exhibit B2-type cubic structure at RT (Figure **14a**), indicating that the temperature of MT is lower than RT. An abrupt magneto-structural transformation (MST) occurs from strong FM austenite to weak magnetic martensite for $Ni_{35}Co_{15-x}Fe_xMn_{35}Ti_{15}$ (x = 2, 4, 6, 8) alloy ribbons in Figure **14b**. As shown in the top right-hand corner of Figure **14b**, the magnetization of FM austenite decreases and T_t increases with decreasing Co/Fe ratio. In all as-prepared ribbons, the $Ni_{35}Co_9Fe_6Mn_{35}Ti_{15}$ ribbon shows the highest ΔS_M and RC. Under magnetic fields of 20 and 50 kOe during reverse MT, the maximum values of ΔS_M/RC reach 9.5(8) J kg^{-1} K^{-1}/79.4(5) J kg^{-1} and 24.0(4) J kg^{-1} K^{-1}/206.8(4) J kg^{-1}, respectively. Huang *et al*. [47] studied the effect of rare earth Y doping on the crystal structure, MT and

MCE of $Mn_{50-x}Y_xNi_{30.5}Co_{9.5}Ti_{10}$ (x = 0, 0.3, 0.5, 0.7) ribbons. Compared with the microstructure of $Mn_{50}Ni_{30.5}Co_{9.5}Ti_{10}$ ribbon (Figure **15a**) at RT, little secondary phase (red arrow) randomly distributing in B2 phase is observed in $Mn_{49.3}Y_{0.7}Ni_{30.5}Co_{9.5}Ti_{10}$ ribbons (Figure **15b**). Figure **15c** shows that the sample exhibits B2 and 5 M phases for x = 0, and main B2 phase with the increase of rare earth Y. At the same time, the MT temperature from ferro- to weak-magnetic state monotonously declines due to the enrichment of rare earth Y-precipitation phase (Figure **15d**). The ΔS_m increased with increasing rare earth Y. The maximum ΔS_m of $Mn_{49.3}Y_{0.7}Ni_{30.5}Co_{9.5}Ti_{10}$ ribbons (Figure **15e**) reaches 6.16 (23.7) J kg^{-1} K^{-1} under 20 (70) kOe.

3.4. Combination of Doping and Texture

Shen *et al*. [66] studied the <001>-oriented $Ni_{35.5}Co_{14.5}Mn_{35}Ti_{15}$ polycrystals prepared by arc-melting and directionally solidification technique. In

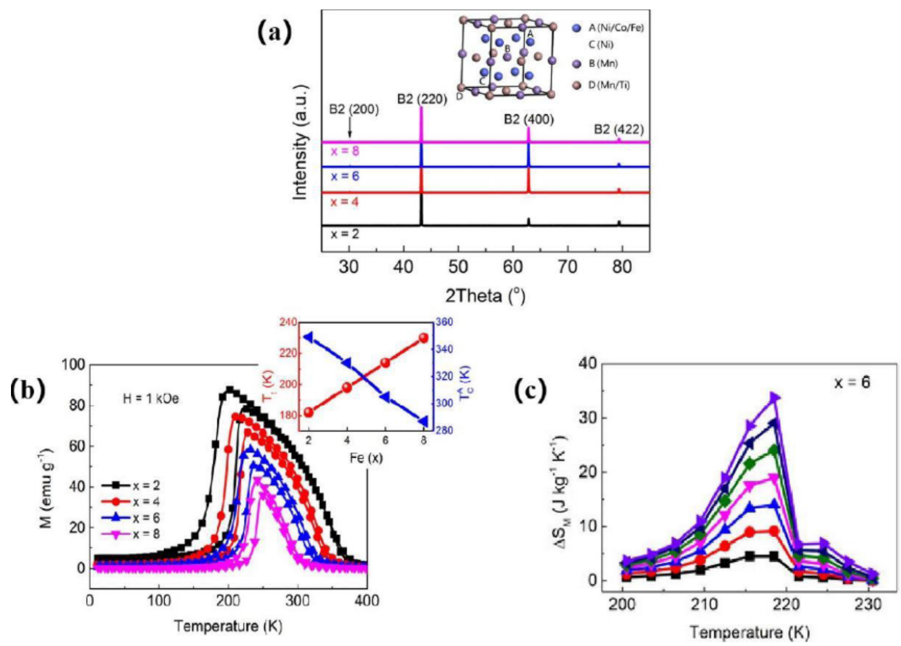

Figure 14: Phase, magnetization and magnetocaloric effect (MCE) of $Ni_{35}Co_{15-x}Fe_xMn_{35}Ti_{15}$ ribbons [51]. (**a**) Room temperature XRD patterns. The inset is the crystal structure and atomic site occupations; (**b**) M-T curves under a field of 1 kOe. The corresponding values of MT temperature (T_t) and Curie temperature of austenite (T_C^A) for samples were displayed; (**c**) The magnetic entropy change ΔS_M as a function of temperature around reverse MT temperature with magnetic fields 10-70 kOe.

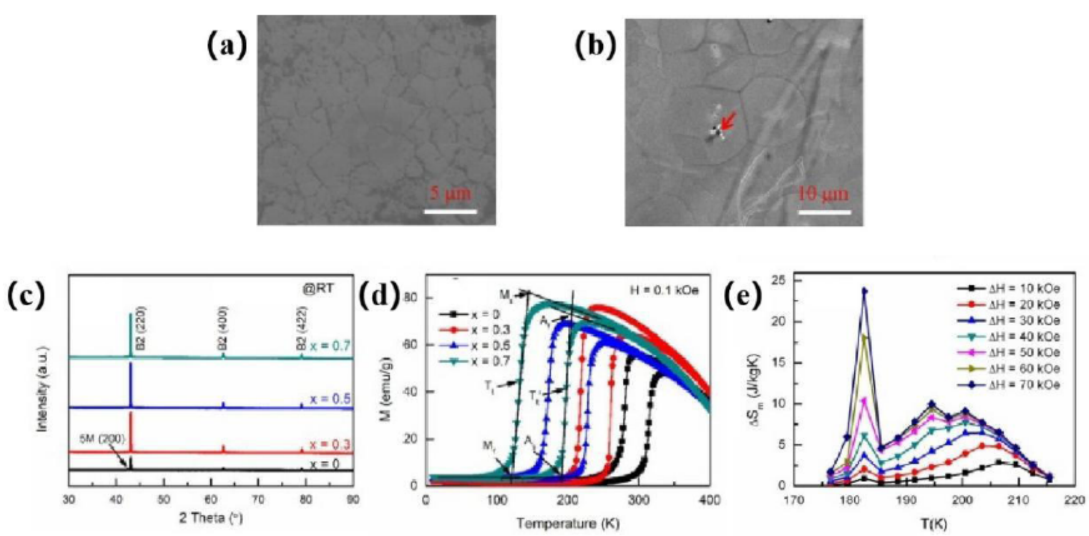

Figure 15: Microstructure, magnetic property and magenetocaloric effects of $Mn_{50-x}Y_xNi_{30.5}Co_{9.5}Ti_{10}$ (x = 0, 0.7) alloy ribbons [47]. (**a, b**) Microstructure on the free surface; (**c**) XRD patterns at RT; (**d**) Temperature dependence of magnetization under a magnetic field of 0.1 kOe; (**e**) Magnetic entropy change (ΔS_m).

Figure **16a**, M_s, M_f, A_s, A_f and ΔT_{Hys} of samples are 292.9, 278.8, 290.8, 301.4 and 10.2 K, respectively. Meanwhile, the corresponding thermal-induced MT entropy change (ΔS_T) could be evaluated to be 42.1 J g^{-1} K^{-1}. Their MT behaviors (Figure **16b**) are similar to that of previously reported non-textured Ni-Co-Mn-Ti alloys [57]. The value of ΔM under a magnetic field of 50 kOe reaches 94 emu g^{-1}. Figure **16c** shows that the specimen subjects to MT at a rather low critical stress (σ_{cr}) of 38 MPa, which produces a transformation strain ($\Delta\varepsilon_{tr}$) of 4%. To complete MT, the applied stress of about 110 MPa is required since MT is not a strictly equilibrium process due to unavoidable nucleation process [7]. The stress hysteresis ($\Delta\sigma_{hy}$) is 54 MPa due to the fact that ambient temperature is close to A_f, leading to a low thermal driving force for the reverse MT. For the loading and unloading stages (Figure **16d**), ΔT_{ad} of 11.5 K and 5.8 K can be obtained. Such an asymmetry in $|\Delta T_{ad}|$ suggests the irreversibility of the eCE between the forward and reverse MT. The main source of the irreversibility is ascribed to the dissipative heat of internal friction caused by the fast interfacial movement upon fast loading/unloading. Compared with other reported first-order elastocaloric materials (Figure **16e**), the <001>-oriented $Ni_{35.5}Co_{14.5}Mn_{35}Ti_{15}$ polycrystalline alloys display excellent eCE. In addition, the results (Figure **16f**) proved that the existence of texture is favorable for improving the eCE performance. Wei *et al*. [67] use the same method to prepare the <001>-oriented $Ni_{35.5}Co_{14.5}Mn_{35}Ti_{15}$ polycrystals. The as-prepared specimen exhibits large barocaloric effect with a ΔS_m of −24.2 J kg^{-1} K^{-1} and an ΔT_{ad} of 4.2 K by the application of a relatively low pressure of 1 kbar.

3.5. Combination of Doping and Multiple External Fields

The applying of multiple external fields may effectively enhance the RC of Heusler alloys [7, 68-70]. Liu *et al*. [45] studied the effect of hydrostatic pressure on MCE of $Ni_{37.5}Co_{12.5}Mn_{35}Ti_{15}$ bulk alloy. The magneto-structural phase transition process is shown in Figure **17a**. Meanwhile, the magnetic field reduces TM temperatures with a rate of -1.4 K T^{-1}. Moreover, the reduction of ΔM across the martensitic transition is observed under hydrostatic pressure (Figure **17b**). At ambient pressure, ΔM reaches 81.3 emu g^{-1} at 7 T under a 10.03 kbar hydrostatic pressure, then it decreases to 54.4 emu g^{-1}. It means that reduction of maximum ΔS_M of $Ni_{37.5}Co_{12.5}Mn_{35}Ti_{15}$ bulk alloy exist under the hydrostatic pressure. The ΔM peak shifts continuously to a higher temperature with increasing hydrostatic pressure. With the application of multi-fields, *i.e*. first applying a magnetic field and withdrawing magnetic field under a hydrostatic

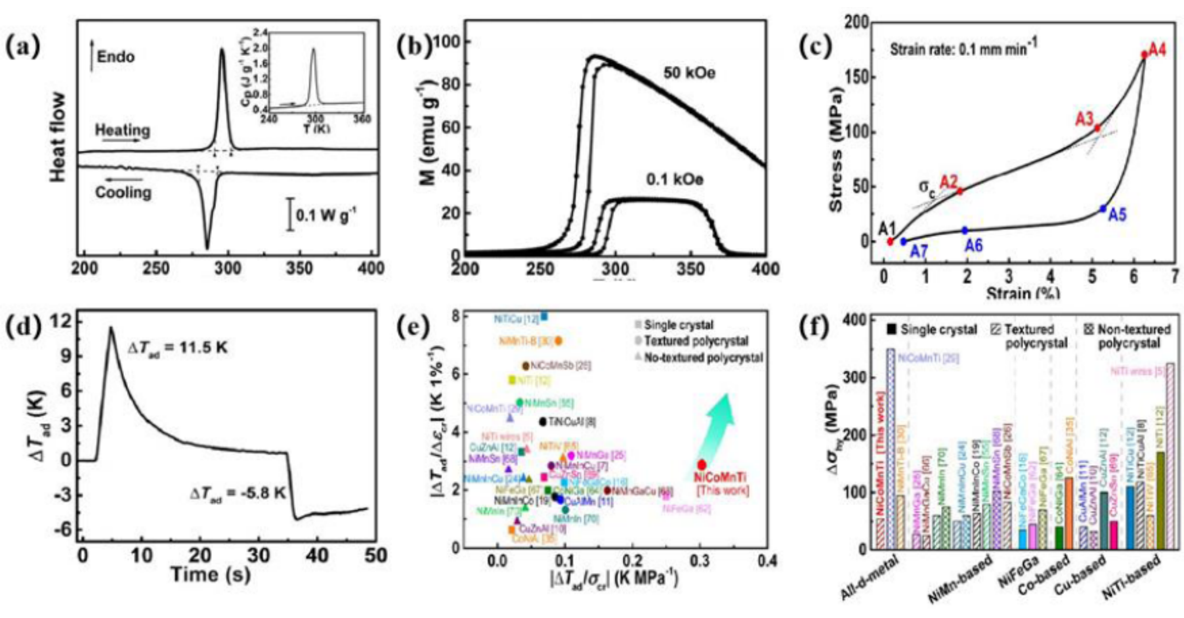

Figure 16: Phase transition, elastocaloric and magnetocaloric effect of polycrystalline $Ni_{35.5}Co_{14.5}Mn_{35}Ti_{15}$ alloys [66]. (**a**) DSC curves of <001>-textured alloys; (**b**) M-T curves under applied fields (μ_0H) of 0.1 and 5 T; (**c**) Stress-strain curve of sample at a strain rate of 0.1 mm/min at 310 K; (**d**) Temperature-time profile; (**e**) Specific adiabatic temperature change *vs* critical stress ($|\Delta T_{ad}/\sigma_{cr}|$) and transformation strain ($|\Delta T_{ad}/\Delta\varepsilon_{tr}|$); (**f**) Stress hysteresis ($\Delta\sigma_{hy}$) for typical room-temperature elastocaloric materials.

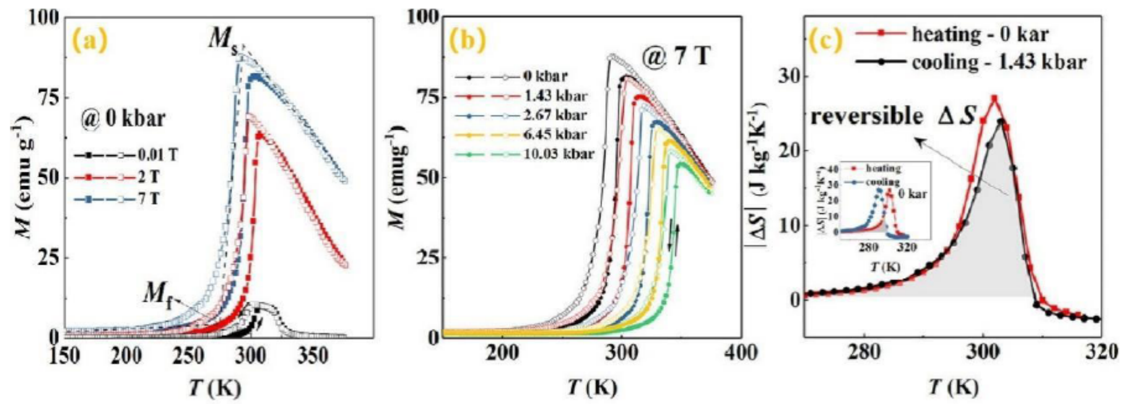

Figure 17: Magnetic properties and magnetocaloric effect of $Ni_{37.5}Co_{12.5}Mn_{35}Ti_{15}$ bulk alloy [45]. (**a**) The Iso-field magnetization curves measure at ambient pressure with magnetic fields 0.01, 2 and 7 T; (**b**) Iso-field magnetization curves measure at fixed magnetic field 7 T under hydrostatic pressures 0, 1.43, 2.67, 6.4, and 10.03 kbar; (**c**) Heating *ΔS-T* curves under ambient pressure and cooling *ΔS-T* curve under hydrostatic pressure of 1.43 kbar under magnetic field changes of 0.01 to 5 T.

pressure, the reversible entropy change increases from 8.9 to 24.1 J $kg^{-1}K^{-1}$ (Figure **17c**) for a magnetic field change from 0.01 to 5 T.

3.6. Combination of Doping, Reducing Sample Size and Multiple External Fields

Li *et al*. [52] applied the hydrostatic pressures in $Ni_{35}Co_{15}Mn_{35-x}Fe_xTi_{15}$ ribbons and systematically investigated the phase transition and magnetocaloric performance. All the samples (Figure **18a**) exhibit magneto-structural phase transition behavior. With increasing Fe content, the T_C^A increases while T_t obviously decreases. Figure **18b** shows the reduction of *ΔM* across the martensitic transition with increasing hydrostatic pressure from 0.25 to 0.75 GPa; the T_t also increases with increasing hydrostatic pressure. These results (Figure **18b**) are similar to that of previously reported Ni-Co-Mn-Ti bulk alloys [45]. In $Ni_{35}Co_{15}Mn_{31}Fe_4Ti_{15}$ Heusler ribbon, the *ΔM* (67.09 emu g^{-1}) under ambient pressure is lower than that under different hydrostatic pressures. By contrast, the *ΔM* (81.3 emu g^{-1}) of sample under ambient pressure is

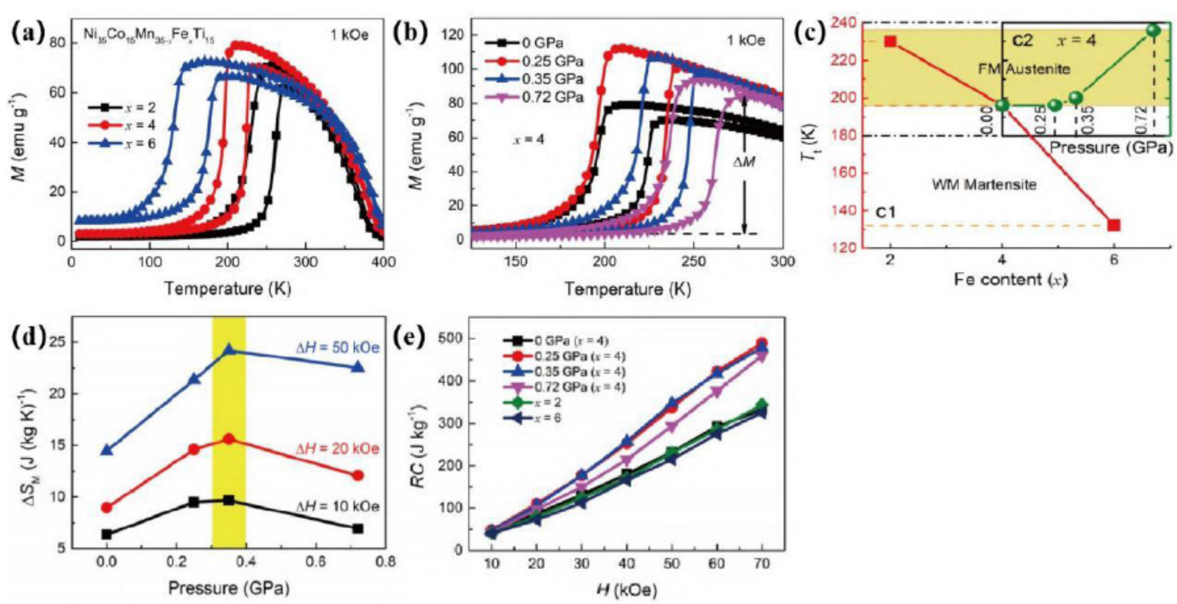

Figure 18: Magnetic properties, phase transition and magnetocaloric effect of $Ni_{35}Co_{15}Mn_{35-x}Fe_xTi_{15}$ (x = 2, 4, 6) ribbons [52]. (**a**) M-T curves under a magnetic field of 1 kOe; (**b**) M-T curves for $Ni_{35}Co_{15}Mn_{31}Fe_4Ti_{15}$ ribbon under a magnetic field of 1 kOe and hydrostatic pressures of 0, 0.25, 0.35 and 0.72 GPa; (**c**) Phase diagrams of (c1) $Ni_{35}Co_{15}Mn_{35-x}Fe_xTi_{15}$ (x = 2, 4, 6) ribbons and (c2) $Ni_{35}Co_{15}Mn_{31}Fe_4Ti_{15}$ ribbon under hydrostatic pressures of 0, 0.25, 0.35 and 0.72 GPa; (**d**) ΔS_M as a function of hydrostatic pressure with magnetic field changes of 10, 20, and 50 kOe; (**e**) Magnetic field dependence of RC with temperatures at full width half-maximum (FWHM) of ΔS_M peaks under hydrostatic pressure.

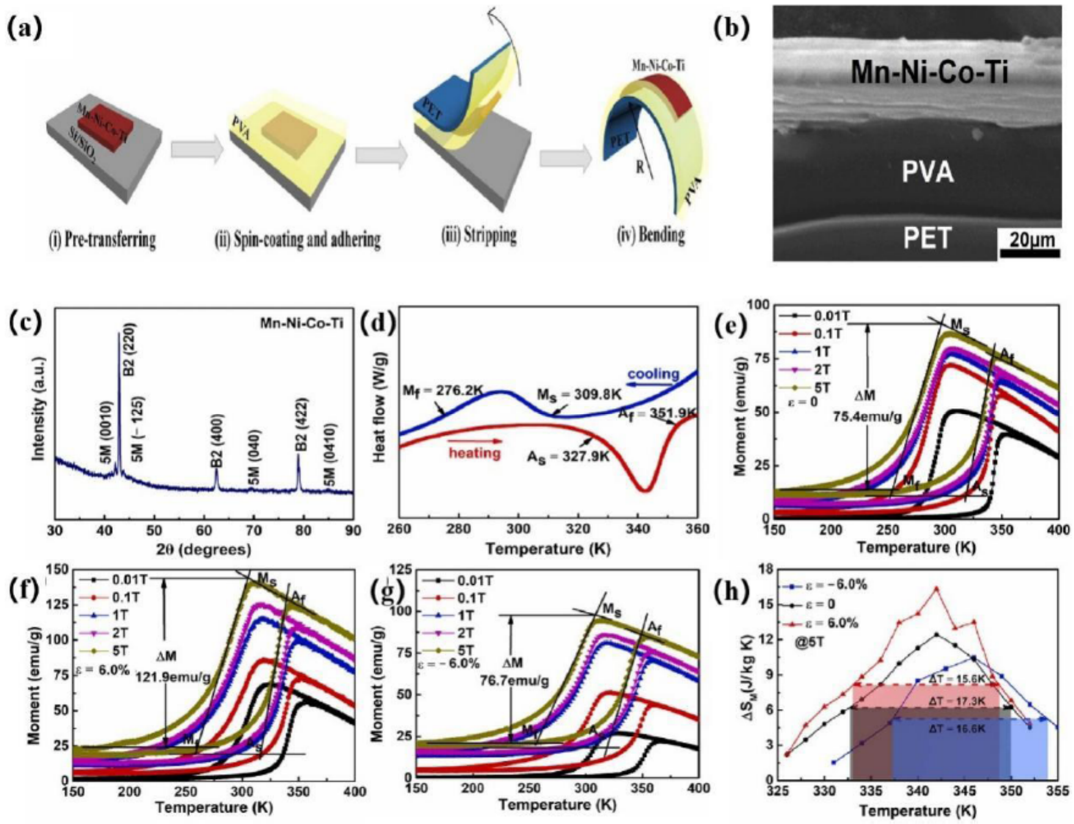

Figure 19: Microstructure and properties of $Mn_{52.6}Ni_{30.5}Co_{7.8}Ti_{9.1}$ composites combined with alloy ribbons, polyvinyl alcohol (PVA) and polyethylene terephthalate (PET) [71]. (**a**) The demonstration of preparation schematic diagram; (**b**) SEM images of the cross section for the $Mn_{52.6}Ni_{30.5}Co_{7.8}Ti_{9.1}$/PVA/PET composite; (**c**) XRD pattern for the $Mn_{52.6}Ni_{30.5}Co_{7.8}Ti_{9.1}$ ribbon; (**d**) DSC curves for the $Mn_{52.6}Ni_{30.5}Co_{7.8}Ti_{9.1}$ ribbon; (**e**) The M-T curves for the $Mn_{52.6}Ni_{30.5}Co_{7.8}Ti_{9.1}$/PVA/PET composite under different magnetic fields; (**f**) The M-T curves for the $Mn_{52.6}Ni_{30.5}Co_{7.8}Ti_{9.1}$/PVA/PET composite in tensile strain state ($\varepsilon = 6.0\%$) under different magnetic fields; (**g**) The M-T curves for the $Mn_{52.6}Ni_{30.5}Co_{7.8}Ti_{9.1}$/PVA/PET composite in compressive strain states ($\varepsilon = -6.0\%$) under different magnetic fields; (**h**) The temperature dependence of isothermal magnetic entropy change (ΔS_M) for the $Mn_{52.6}Ni_{30.5}Co_{7.8}Ti_{9.1}$ ribbon with the variation of the magnetic field from 0 to 5 T under different strain states.

higher than that under hydrostatic pressure in $Ni_{37.5}Co_{12.5}Mn_{35}Ti_{15}$ bulk alloy. This may be attributed to the composition and microstructure difference of the ribbon and bulk alloys. In Figure **18c**, the combined doping and hydrostatic pressures change the MST of all-d-metal alloys, shifting the MST to the desired temperature rang. As depicted in Figure **18d** and **e**, the $Ni_{35}Co_{15}Mn_{31}Fe_4Ti_{15}$ ribbon exhibits the best magnetocaloric performance under hydrostatic pressures of 0.35 GPa. The maximum values of ΔS_M (RC) are 15.61 J $kg^{-1}K^{-1}$ (109.91 J kg^{-1}) and 24.2 J $kg^{-1}K^{-1}$ (347.26 J kg^{-1}) under 20 and 50 kOe, respectively. Zhao *et al*. [71] fabricated novel flexible composites (Figure **19a**) by combining $Mn_{52.6}Ni_{30.5}Co_{7.8}Ti_{9.1}$ ribbons, polyvinyl alcohol (PVA) and polyethylene terephthalate (PET). Figure **19b** clearly reveals the compact contact interfaces of Mn-Ni-Co-Ti/PVA/PET flexible composite. The two-phase coexistence of B2-type and five-layer modulated (5 M) structure (Figure **19c**) indicates that the MT temperature of ribbons is around RT. In Figure **19d**, the related temperatures of MT (M_s, M_f, A_s and A_f) are 309.8 K, 276.2 K, 327.9 K and 351.9 K, respectively. On the other hand, the ΔT_{Hys} and ΔT_{Int} are calculated to be 46.9 and 28.5 K, respectively. Figure **19e**-**g** show the different ΔM across the martensitic transition in different strain states at a magnetic field of 5 T. Compared with the ΔM (75.4 emu g^{-1}) under zero strain ($\varepsilon = 0$), the ΔM under higher strain ($\varepsilon =$ 6.0%) is obviously higher. The peak of ΔS_M (Figure **19h**) under 5 T is 12.44, 16.34 and 10.48 J kg^{-1} K^{-1} at strains (ε) of 0%, 6.0% and -6.0%, respectively. At the same time, the maximum RC obtained at three different strains (ε) of 0%, 6.0% and -6.0% is 157.02, 197.35 and 109.12 J kg^{-1}, respectively.

4. SUMMARY AND PERSPECTIVES

The traditional Heusler alloys dispaly poor mechanical properties (especially low ductility) due to the existence of covalent bond formed via p-d orbital hybridization in the parent phase. In order to overcome the drawback of traditional Heusler alloys and improve their practical applications, Wei *et al*. firstly prepared a novel Heusler alloy (Ni-Mn-Ti, named all-d-metal Heusler alloy) by only transition metal elements in 2015; it exhibited great mechanical properties because of the replacement of strong p-d hybridization by relatively weaker d-d hybridization in Ni-Mn-Ti Heusler alloy. Meanwhile, the Ni-Mn-Ti all-d-metal Heusler alloy showed large transition entropy changes and large volume changes across the martensitic transition. These features resulted in miraculously mechano-caloric effects of Ni-Mn-Ti Heusler alloy. Unfortunately, there were still some defects affecting the actual applications of Ni-Mn-Ti or Mn-Ni-Ti all-d-metal alloys. Researchers have invested great effort and employed some strategies to solve these problems, including (a) element doping, (b) microstructure adjustment (texture and reducing sample size) and (c) multi-field cooperation. All studies of all-d-metal alloys demonstrated that they may act as promising candidate materials for solid state refrigeration at ambient temperature. However, the present studies mainly focused on the bulk state, and few works on small-sized ribbons. In addition, most of the works concentrate on the magnetocaloric effects rather than elastocaloric effect. Finally, the mechanical properties (especially the ductility enhancement and related mechanisms), have not been systematically investigated.

Future research perspectives on all-d-metal Heusler alloys lie on optimization of the composition, microstructure and preparation techniques. The corresponding properties, including mechanical, magnetic and refrigeration performance are crucial for their critical applications. These include:

(a) Compositional optimization, based on the mechanical, magnetic, martensite transformation and related properties, is necessary for the enrichment of the alloy system. Some new design techniques such as computational simulation combined with high throughput experimental method may be promising;

(b) Preparation and properties of small sized materials including wires, films and powders may render all-d-metal alloys new advantages for new properties and also applications. The magnetic hysteresis may be reduced via reducing the materials size, which may effectively enhance the reversibility during solid state refrigeration cycling. The small-sized materials may also act as building-blocks for complex shaped structures used for solid-state refrigeration, in which the large specific surface area of small-size materials improve the heat exchange capacity between the working material and flowing reagent.

(c) Elastocaloric effect, driving by external mechanical stress, may be promising for all-d-metal alloys, supposing that these alloys exhibit high enough strength as well as ductility. Systematic studies on the toughening mechanisms of these alloys become necessary. On the other hand, the combination of magnetocaloric and elastocaloric effects is also important for their application for room-temperature refrigeration.

LIST OF ABBREVIATIONS

MCE	magnetocaloric effect
eCE	elastocaloric effect
BCE	barocaloric effect
MR	magnetoresistance
MT	martensite transformation
FMMT	ferromagnetic martensite transformation
FOMT	first-order magnetic transition
IMT	intermartensite transformation
MST	magneto-structural transformation
AFM	antiferromagnetic
PM	paramagnetic
FM	ferromagnetic
M_s	the starting temperatures of forward MT
M_f	the finishing temperatures of forward MT
A_s	the starting temperatures of inverse MT
A_f	the finishing temperatures of inverse MT
T_t	temperature of MT
T_C^A	Curie temperature of austenite
ΔH	latent heat
ΔM	magnetization difference
ΔS_m	magnetic entropy changes
ΔT_{ad}	adiabatic temperature change
ΔS_{iso}	isothermal entropy change
ΔT_{Hys}	thermal hysteresis
ΔT_{Int}	phase transition interval
ε	strains

$\Delta\varepsilon_{tr}$	transformation strain
σ_{cr}	critical stress
$\Delta\sigma_{hy}$	stress hysteresis
RC	refrigeration capacity
OM	optical microscopy
SEM	scanning electron microscopy
TEM	transmission electron microscopy
XRD	X-ray diffraction
DSC	differential scanning calorimetry
DC	direct-current
DT	deposition temperature
RT	room temperature
PVA	polyvinyl alcohol
PET	polyethylene terephthalate

ACKNOWLEDGEMENT

Financial supports from Guangdong Province Key Area R&D Program (Grant Number 2019B010942001) and Heilongjiang Touyan Team are greatly acknowledged.

CONFLICT OF INTEREST

The authors declare that they have no known competing financial interests or personal relationships that could have appeared to influence the work reported in this paper.

REFERENCE

[1] R. Kainuma, Y. Imano, W. Ito, Y. Sutou, H. Morito, S. Okamoto, O. Kitakami, K. Oikawa, A. Fujita, T. Kanomata, K. Ishida, Magnetic-field-induced shape recovery by reverse phase transformation, Nature 439(7079) (2006) 957-960. https://doi.org/10.1038/nature04493

[2] I. Suorsa, J. Tellinen, K. Ullakko, E. Pagounis, Voltage generation induced by mechanical straining in magnetic shape memory materials, Journal of Applied Physics 95(12) (2004) 8054-8058. https://doi.org/10.1063/1.1711181

[3] I. Karaman, B. Basaran, H.E. Karaca, A.I. Karsilayan, Y.I. Chumlyakov, Energy harvesting using martensite variant reorientation mechanism in a NiMnGa magnetic shape memory alloy, Applied Physics Letters 90(17) (2007) 172505. https://doi.org/10.1063/1.2721143

[4] V. Srivastava, Y.T. Song, K. Bhatti, R.D. James, The direct conversion of heat to electricity using multiferroic alloys, Advanced Energy Materials 1(1) (2011) 97-104. https://doi.org/10.1002/aenm.201000048

[5] L. Pfeuffer, J. Lemke, N. Shayanfar, S. Riegg, D. Koch, A. Taubel, F. Scheibel, N.A. Kani, E. Adabifiroozjaei, L. Molina-Luna, K.P. Skokov, O. Gutfleisch, Microstructure engineering of metamagnetic Ni-Mn-based Heusler compounds by Fe-doping: A roadmap towards excellent cyclic stability combined with large elastocaloric and magnetocaloric effects, Acta Materialia 221 (2021) 117390. https://doi.org/10.1016/j.actamat.2021.117390

[6] M.T. Khan, Y. Wang, C. Wang, X.Q. Liao, S. Yang, X.P. Song, X.B. Ren, Combination of conventional elastocaloric and magnetocaloric effects in a Co37Ni35Al28 ferromagnetic shape memory alloy, Scripta Materialia 146 (2018) 182-186. https://doi.org/10.1016/j.scriptamat.2017.11.041

[7] L. Mañosa, A. Planes, Materials with Giant Mechanocaloric Effects: Cooling by Strength, Advanced Materials 29(11) (2017) 1603607. https://doi.org/10.1002/adma.201603607

[8] Y.H. Qu, D.Y. Cong, X.M. Sun, Z.H. Nie, W.Y. Gui, R.G. Li, Y. Ren, Y.D. Wang, Giant and reversible room-temperature magnetocaloric effect in Ti-doped Ni-Co-Mn-Sn magnetic shape memory alloys, Acta Materialia 134 (2017) 236-248. https://doi.org/10.1016/j.actamat.2017.06.010

[9] S.B. Sun, H.X. Qin, L.J. Kong, R. Ning, Y.D. Zhao, Z.Y. Gao, W. Cai, Defect engineering: electron-exchange integral manipulation to generate a large magnetocaloric effect in Ni41Mn43Co6Sn10 alloys, ACS Applied Materials & Interfaces 13 (48) (2021) 57372-57379. https://doi.org/10.1021/acsami.1c18587

[10] D. Li, Z.B. Li, X.L. Zhang, C. Liu, G.Y. Zhang, J.J. Yang, B. Yang, H.L. Yan, D.Y. Cong, X. Zhao, L. Zuo, Giant elastocaloric effect in Ni-Mn-Ga-based alloys boosted by a large lattice volume change upon the martensitic transformation, ACS Applied Materials & Interfaces 14 (1) (2022) 1505-1518. https://doi.org/10.1021/acsami.1c22235

[11] Y. Li, W. Sun, D.W. Zhao, H. Xu, J. Liu, An 8 K elastocaloric temperature change induced by 1.3% transformation strain in Ni44Mn45-xSn11Cux alloys, Scripta Materialia 130 (2017) 278-282. https://doi.org/10.1016/j.scriptamat.2016.12.014

[12] A. Aznar, A. Gràcia-Condal, A. Planes, P. Lloveras, M. Barrio, J.-L. Tamarit, W.X. Xiong, D.Y. Cong, C. Popescu, L. Mañosa, Giant barocaloric effect in all-d-metal Heusler shape memory alloys, Physical Review Materials 3(4) (2019) 044406. https://doi.org/10.1103/PhysRevMaterials.3.044406

[13] M.Q. Yu, G.W. Li, C.G. Fu, E.K. Liu, K. Manna, E. Budiyanto, Q. Yang, C. Felser, H. Tuysuz, Tunable eg orbital occupancy in Heusler compounds for oxygen evolution reaction, Angewandte Chemie International Edition 60(11) (2021) 5800-5805. https://doi.org/10.1002/anie.202013610

[14] T. Kojima, S. Kameoka, A. P. Tsai, The emergence of Heusler alloy catalysts, Science and Technology of Advanced Materials 20(1) (2019) 445-455. https://doi.org/10.1080/14686996.2019.1598238

[15] Y. Nishino, M. Kato, S. Asano, K. Soda, M. Hayasaki, U. Mizutani, Semiconductorlike behavior of electrical resistivity in Heusler-type Fe2VAl, Physical Review Letters 79 (1997) 1909-1912. https://doi.org/10.1103/PhysRevLett.79.1909

[16] D. Sprungmann, K. Westerholt, H. Zabel, M. Weides, H. Kohlstedt, Evidence for triplet superconductivity in Josephson junctions with barriers of the ferromagnetic Heusler alloy Cu2MnAl, Physical Review B 82(6) (2010) 060505. https://doi.org/10.1103/PhysRevB.82.060505

[17] T. Mizuno, Y. Tsuchiya, T. Machita, S. Hara, D. Miyauchi, K. Shimazawa, T. Chou, K. Noguchi, K. Tagami, Transport and magnetic properties of CPP-GMR sensor with CoMnSi Heusler alloy, IEEE Transactions on Magnetics 44(11) (2008) 3584-3587. https://doi.org/10.1109/TMAG.2008.2001655

[18] P. Khunkitti, A. Siritaratiwat, K. Pituso, Free layer thickness dependence of the stability in Co2(Mn0.6Fe0.4)Ge Heusler

based CPP-GMR read sensor for areal density of 1 Tb/In(2), Micromachines (Basel) 12(9) (2021) 1010. https://doi.org/10.3390/mi12091010

[19] S.Y. Yu, Z.H. Liu, G.D. Liu, J.L. Chen, Z.X. Cao, G.H. Wu, B. Zhang, X.X. Zhang, Large magnetoresistance in single-crystalline Ni50Mn50−xInx alloys (x=14-16) upon martensitic transformation, Applied Physics Letters 89(16) (2006) 162503. https://doi.org/10.1063/1.2362581

[20] K. Ullakko, J.K. Huang, C. Kantner, R.C. O'Handley, V.V. Kokorin, Large magnetic-field-induced strains in Ni2MnGa single crystals, Applied Physics Letters 69(13) (1996) 1966-1968. https://doi.org/10.1063/1.117637

[21] T. Graf, C. Felser, S.S.P. Parkin, Simple rules for the understanding of Heusler compounds, Progress in Solid State Chemistry 39(1) (2011) 1-50. https://doi.org/10.1016/j.progsolidstchem.2011.02.001

[22] U. Adem, I. Dincer, S. Aktürk, M. Acet, Y. Elerman, Phase formation characteristics and magnetic properties of bulk Ni2MnGe Heusler alloy, Journal of Alloys and Compounds 618 (2015) 115-119. https://doi.org/10.1016/j.jallcom.2014.08.149

[23] Y. Chieda, T. Kanomata, K. Fukushima, K. Matsubayashi, Y. Uwatoko, R. Kainuma, K. Oikawa, K. Ishida, K. Obara, T. Shishido, Magnetic properties of Mn-rich Ni2MnSn Heusler alloys under pressure, Journal of Alloys and Compounds 486(1-2) (2009) 51-54. https://doi.org/10.1016/j.jallcom.2009.06.206

[24] C.D. Gelatt, A.R. Williams, V.L. Moruzzi, Theory of bonding of transition metals to nontransition metals, Physical Review B 27(4) (1983) 2005-2013. https://doi.org/10.1103/PhysRevB.27.2005

[25] T. Cao, H.C. Xuan, S.L. Liu, L.B. Wang, Z.G. Xie, X.H. Liang, F.H. Chen, P.D. Han, D.H. Wang, Y.W. Du, Enhanced elastocaloric effect and mechanical properties of Fe-doped Ni-Mn-Al ferromagnetic shape memory alloys, Intermetallics 112 (2019) 106529. https://doi.org/10.1016/j.intermet.2019.106529

[26] J.M. Wang, C.B. Jiang, A single-phase wide-hysteresis shape memory alloy Ni50Mn25Ga17Cu8, Scripta Materialia 62(5) (2010) 298-300. https://doi.org/10.1016/j.scriptamat.2009.11.023

[27] A.A. Cherechukin, I.E. Dikshtein, D.I. Ermakov, A.V. Glebov, V.V. Koledov, D.A. Kosolapov, V.G. Shavrov, A.A. Tulaikova, E.P. Krasnoperov, T. Takagi, Shape memory effect due to magnetic field-induced thermoelastic martensitic transformation in polycrystalline Ni-Mn-Fe-Ga alloy, Physics Letters A 291 (2001) 175-183. https://doi.org/10.1016/S0375-9601(01)00688-0

[28] Y.Q. Ma, S.Y. Yang, Y. Liu, X.J. Liu, The ductility and shape-memory properties of Ni-Mn-Co-Ga high-temperature shape-memory alloys, Acta Materialia 57(11) (2009) 3232-3241. https://doi.org/10.1016/j.actamat.2009.03.025

[29] N.V. Nong, L.T. Tai, N.T. Huy, N.T. Trung, C.R.H. Bahl, R. Venkatesh, F.W. Poulsen, N. Pryds, Structural, magnetic and magnetocaloric properties of Heusler alloys Ni50Mn38Sb12 with boron addition, Materials Science and Engineering: B 176(16) (2011) 1322-1325. https://doi.org/10.1016/j.mseb.2011.07.013

[30] Z. Yang, D.Y. Cong, X.M. Sun, Z.H. Nie, Y.D. Wang, Enhanced cyclability of elastocaloric effect in boron-microalloyed Ni-Mn-In magnetic shape memory alloys, Acta Materialia 127 (2017) 33-42. https://doi.org/10.1016/j.actamat.2017.01.025

[31] K. Tsuchiya, A. Tsutsumi, H. Ohtsuka, M. Umemoto, Modification of Ni-Mn-Ga ferromagnetic shape memory alloy by addition of rare earth elements, Materials Science and Engineering: A 378(1-2) (2004) 370-376. https://doi.org/10.1016/j.msea.2003.11.076

[32] G.F. Dong, H.J. Zhang, X.L. Zhang, H.B. Wang, J.H. Sui, W. Cai, Microstructure and mechanical properties in Ni45.4Mn39.5In13.1Gd2 alloy with high transformation temperature, Materials Science and Technology 28(11) (2014) 1332-1336. https://doi.org/10.1179/1743284712Y.0000000070

[33] W. Cai, L. Gao, A.L. Liu, J.H. Sui, Z.Y. Gao, Martensitic transformation and mechanical properties of Ni-Mn-Ga-Y ferromagnetic shape memory alloys, Scripta Materialia 57(7) (2007) 659-662. https://doi.org/10.1016/j.scriptamat.2007.05.041

[34] X.H. Tian, K. Zhang, C.L. Tan, E.J. Guo, Influence of Doping Tb on the Mechanical Properties and Martensitic Transformation of Ni-Mn-Sn Magnetic Shape Memory Alloys, Crystals 8(6) (2018) 247. https://doi.org/10.3390/cryst8060247

[35] Y.J. Huang, Q.D. Hu, N.M. Bruno, J.-H. Chen, I. Karaman, J.H. Ross, J.G. Li, Giant elastocaloric effect in directionally solidified Ni-Mn-In magnetic shape memory alloy, Scripta Materialia 105 (2015) 42-45. https://doi.org/10.1016/j.scriptamat.2015.04.024

[36] D.W. Zhao, J. Liu, X. Chen, W. Sun, Y. Li, M.X. Zhang, Y.Y. Shao, H. Zhang, A.R. Yan, Giant caloric effect of low-hysteresis metamagnetic shape memory alloys with exceptional cyclic functionality, Acta Materialia 133 (2017) 217-223. https://doi.org/10.1016/j.actamat.2017.05.020

[37] Y.J. Huang, Q.D. Hu, J. Liu, L. Zeng, D.F. Zhang, J.G. Li, Banded-like morphology and martensitic transformation of dual-phase Ni-Mn-In magnetic shape memory alloy with enhanced ductility, Acta Materialia 61(15) (2013) 5702-5712. https://doi.org/10.1016/j.actamat.2013.06.012

[38] Y. Zhang, M. Li, Y.D. Wang, J.P. Lin, K.A. Dahmen, Z.L. Wang, P.K. Liaw, Superelasticity and Serration Behavior in Small-Sized NiMnGa Alloys, Advanced Engineering Materials 16(8) (2014) 955-960. https://doi.org/10.1002/adem.201300518

[39] D.C. Dunand, P. Müllner, Size effects on magnetic actuation in Ni-Mn-Ga shape-memory alloys, Advanced Materials 23(2) (2011) 216-32. https://doi.org/10.1002/adma.201002753

[40] Y. Feng, H. Chen, L. Gao, H.B. Wang, X.H. Bian, M.J. Gong, Effect of wheel speed and annealing temperature on microstructure and texture evolution of Ni45Mn36.6In13.4Co5 ribbon, Materials Characterization 122 (2016) 170-176. https://doi.org/10.1016/j.matchar.2016.10.030

[41] Z.Y. Wei, E.K. Liu, J.H. Chen, Y. Li, G.D. Liu, H.Z. Luo, X.K. Xi, H.W. Zhang, W.H. Wang, G.H. Wu, Realization of multifunctional shape-memory ferromagnets in all-d-metal Heusler phases, Applied Physics Letters 107(2) (2015) 022406. https://doi.org/10.1063/1.4927058

[42] A. Taubel, B. Beckmann, L. Pfeuffer, N. Fortunato, F. Scheibel, S. Ener, T. Gottschall, K.P. Skokov, H.B. Zhang, O. Gutfleisch, Tailoring magnetocaloric effect in all-d-metal Ni-Co-Mn-Ti Heusler alloys: a combined experimental and theoretical study, Acta Materialia 201 (2020) 425-434. https://doi.org/10.1016/j.actamat.2020.10.013

[43] Z.Y. Wei, E.K. Liu, Y. Li, X.L. Han, Z.W. Du, H.Z. Luo, G.D. Liu, X.K. Xi, H.W. Zhang, W.H. Wang, G.H. Wu, Magnetostructural martensitic transformations with large volume changes and magneto-strains in all-d-metal Heusler alloys, Applied Physics Letters 109(7) (2016) 071904. https://doi.org/10.1063/1.4961382

[44] H.L. Yan, L.D. Wang, H.X. Liu, X.M. Huang, N. Jia, Z.B. Li, B. Yang, Y.D. Zhang, C. Esling, X. Zhao, L. Zuo, Giant elastocaloric effect and exceptional mechanical properties in an all-d-metal Ni-Mn-Ti alloy: Experimental and ab-initio

studies, Materials & Design 184 (2019) 108180. https://doi.org/10.1016/j.matdes.2019.108180

[45] Y. Liu, A.D. Xiao, T.Z. Yang, Z.T. Xu, X.L. Zhou, T.Y. Ma, Enhancing reversible entropy change of all-d-metal Ni37.5Co12.5Mn35Ti15 alloy by multiple external fields, Scripta Materialia 207 (2022) 114303. https://doi.org/10.1016/j.scriptamat.2021.114303

[46] D.Y. Cong, W.X. Xiong, A. Planes, Y. Ren, L. Manosa, P.Y. Cao, Z.H. Nie, X.M. Sun, Z. Yang, X.F. Hong, Y.D. Wang, Colossal elastocaloric effect in ferroelastic Ni-Mn-Ti alloys, Physical review letters 122(25) (2019) 255703. https://doi.org/10.1103/PhysRevLett.122.255703

[47] S.Y. Huang, L. Qin, Y. Li, L.W. Li, The study of martensitic transformation and magnetocaloric effect in rare earth Y-doped all-d-metal Ni-Co-Mn-Ti Heusler alloys, Materials Letters 302 (2021) 130376. https://doi.org/10.1016/j.matlet.2021.130376

[48] K. Liu, S.C. Ma, C.C. Ma, X.Q. Han, K. Yu, S. Yang, Z.S. Zhang, Y. Song, X.H. Luo, C.C. Chen, S.U. Rehman, Z.C. Zhong, Martensitic transformation and giant magneto-functional properties in all-d-metal Ni-Co-Mn-Ti alloy ribbons, Journal of Alloys and Compounds 790 (2019) 78-92. https://doi.org/10.1016/j.jallcom.2019.03.173

[49] K. Liu, X.Q. Han, K. Yu, C.C. Ma, Z.S. Zhang, Y. Song, S.C. Ma, H. Zeng, C.C. Chen, X.H. Luo, S.U. Rehman, Z.C. Zhong, Magnetic-field-induced metamagnetic reverse martensitic transformation and magnetocaloric effect in all-d-metal Ni36.0Co14.0Mn35.7Ti14.3 alloy ribbons, Intermetallics 110 (2019) 106472. https://doi.org/10.1016/j.intermet.2019.106472

[50] H. Neves Bez, A.K. Pathak, A. Biswas, N. Zarkevich, V. Balema, Y. Mudryk, D.D. Johnson, V.K. Pecharsky, Giant enhancement of the magnetocaloric response in Ni-Co-Mn-Ti by rapid solidification, Acta Materialia 173 (2019) 225-230. https://doi.org/10.1016/j.actamat.2019.05.004

[51] Y. Li, S.Y. Huang, W.H. Wang, E.K. Liu, L.W. Li, Ferromagnetic martensitic transformation and large magnetocaloric effect in Ni35Co15−xFexMn35Ti15 (x = 2, 4, 6, 8) alloys, Journal of Applied Physics 127 (2020) 233907. https://doi.org/10.1063/5.0001403

[52] Y. Li, L. Qin, S.Y. Huang, L.W. Li, Enhanced magnetocaloric performances and tunable martensitic transformation in Ni35Co15Mn35−xFexTi15 all-d-metal Heusler alloys by chemical and physical pressures, Science China Materials 65 (2022) 486-493. https://doi.org/10.1007/s40843-021-1747-3

[53] Q.Q. Zeng, J.L. Shen, H.N. Zhang, J. Chen, B. Ding, X.K. Xi, E.K. Liu, W.H. Wang, G.H. Wu, Electronic behaviors during martensitic transformations in all-d-metal Heusler alloys, Journal of Physics: Condensed Matter 31(42) (2019) 425401. https://doi.org/10.1088/1361-648X/ab2bd8

[54] K. Liu, S.C. Ma, Z.S. Zhang, X.W. Zhao, B. Yang, D.H. Wang, S. Ur Rehman, Z.C. Zhong, Giant exchange bias effect in all-3d-metal Ni38.8Co2.9Mn37.9Ti20.4 thin film, Applied Physics Letters 116(2) (2020) 022412. https://doi.org/10.1063/1.5129878

[55] K. Yu, K. Liu, S.C. Ma, X.Q. Han, Z.S. Zhang, Y. Song, Y.X. Zhang, C.C. Chen, X.H. Luo, Z.C. Zhong, Dependence of microstructure and magnetism on deposition temperature in Ni-Co-Mn-Ti all-d Heusler alloy thin films, Journal of Magnetism and Magnetic Materials 484 (2019) 31-36. https://doi.org/10.1016/j.jmmm.2019.03.119

[56] V.G. de Paula, L.S. de Oliveira, A.A. Mendes Filho, C.T. Rios, J.A. Souza, Thermal annealing influence on structural, magnetic, electronic, and mechanical properties of off-stoichiometric Ni40Cu10Mn35Ti15 all-d-metal Heusler alloy, Journal of Materials Research 35(21) (2020) 3004-3011. https://doi.org/10.1557/jmr.2020.217

[57] Z.Y. Wei, W. Sun, Q. Shen, Y. Shen, Y.F. Zhang, E.K. Liu, J. Liu, Elastocaloric effect of all-d-metal Heusler NiMnTi(Co) magnetic shape memory alloys by digital image correlation and infrared thermography.pdf, Applied Physics Letters 114 (2019) 101903. https://doi.org/10.1063/1.5077076

[58] S.L. Liu, H.C. Xuan, T. Cao, L.B. Wang, Z.G. Xie, X.H. Liang, H. Li, L. Feng, F.H. Chen, P.D. Han, Magnetocaloric and elastocaloric effects in all-d-Metal Ni37Co9Fe4Mn35Ti15 magnetic shape memory alloy, Physica Status Solidi (a) 216(23) (2019) 1900563. https://doi.org/10.1002/pssa.201900563

[59] Y.H. Qu, D.Y. Cong, S.H. Li, W.Y. Gui, Z.H. Nie, M.H. Zhang, Y. Ren, Y.D. Wang, Simultaneously achieved large reversible elastocaloric and magnetocaloric effects and their coupling in a magnetic shape memory alloy, Acta Materialia 151 (2018) 41-55. https://doi.org/10.1016/j.actamat.2018.03.031

[60] Y. Shen, W. Sun, Z.Y. Wei, Q. Shen, Y.F. Zhang, J. Liu, Orientation dependent elastocaloric effect in directionally solidified Ni-Mn-Sn alloys, Scripta Materialia 163 (2019) 14-18. https://doi.org/10.1016/j.scriptamat.2018.12.026

[61] W. Sun, J. Liu, D.W. Zhao, M.X. Zhang, Directional solidification and elastocaloric effect in a Ni45Mn44Sn11 magnetic shape memory alloy, Journal of Physics D: Applied Physics 50(44) (2017) 444001. https://doi.org/10.1088/1361-6463/aa87ef

[62] A. Shen, W. Sun, D.W. Zhao, J. Liu, Influence of Cr on microstructure and elastocaloric effect in Ni-Mn-In-Co-Cr polycrystalline alloys, Physics Letters A 382 (2018) 2876-2879. https://doi.org/10.1016/j.physleta.2018.06.022

[63] S. Hattori, R. Ishikura, Q.L. Zhang, Construction of database on cavitation erosion and analyses of carbon steel data, Wear 257(9-10) (2004) 1022-1029. https://doi.org/10.1016/j.wear.2004.07.002

[64] R.S. Xing, D.J. Yu, G.F. Xie, Z.H. Yang, X.X. Wang, X. Chen, Effect of thermal aging on mechanical properties of a Bainitic forging steel for reactor pressure vessel, Materials Science and Engineering: A 720 (2018) 169-175. https://doi.org/10.1016/j.msea.2018.02.036

[65] A. Lara-Guevara, I. Rojas-Rodríguez, C.J. Ortiz-Echeverri, M. Robles-Agudo, M.E. Rodríguez-García, Thermal, structural, and microstructural characterization of eutectoid steel at different heat treatments, Journal of Materials Research 32(11) (2017) 2202-2209. https://doi.org/10.1557/jmr.2017.47

[66] Y. Shen, Z.Y. Wei, W. Sun, Y.F. Zhang, E.K. Liu, J. Liu, Large elastocaloric effect in directionally solidified all-d-metal Heusler metamagnetic shape memory alloys, Acta Materialia 188 (2020) 677-685. https://doi.org/10.1016/j.actamat.2020.02.045

[67] Z.Y. Wei, Y. Shen, Z. Zhang, J.P. Guo, B. Li, E.K. Liu, Z.D. Zhang, J. Liu, Low-pressure-induced giant barocaloric effect in an all-d-metal Heusler Ni35.5Co14.5Mn35Ti15 magnetic shape memory alloy, APL Materials 8(5) (2020) 051101. https://doi.org/10.1063/5.0005021

[68] L. Mañosa, A. Planes, M. Acet, Advanced materials for solid-state refrigeration, Journal of Materials Chemistry A 1(16) (2013) 4925. https://doi.org/10.1039/c3ta01289a

[69] Y.Y. Gong, D.H. Wang, Q.Q. Cao, E.K. Liu, J. Liu, Y.W. Du, Electric field control of the magnetocaloric effect, Advanced materials 27(5) (2015) 801-5. https://doi.org/10.1002/adma.201404725

[70] L. Jian, Tino Gottschall, Konstantin P Skokov, James D Moore, Oliver Gutfleisch, Giant magnetocaloric effect driven by structural transitions, Nature materials 11(7) (2012) 620-6. https://doi.org/10.1038/nmat3334

[71] X.Y. Zhao, Y.X. Yan, J.H. Wen, Y. Li, L.W. Li, Enhancement of magnetocaloric effect in all-d-metal Heusler Mn52.6Ni30.5Co7.8Ti9.1/PVA/PET flexible composite by mechanical strains, Journal of Alloys and Compounds 897 (2022) 163116. https://doi.org/10.1016/j.jallcom.2021.163116

Received on 27-07-2022 Accepted on 02-09-2022 Published on 19-10-2022

DOI: https://doi.org/10.31875/2410-2199.2022.09.06